Glacial and environmental changes in northern Svalbard over the last 16.3 ka inferred from neodymium isotopes

Kwangchul Jang [a], Youngkyu Ahn [a], Young Jin Joe [a], Carmen A. Braun [b], Young Ji Joo [a,1], Jung-Hyun Kim [a], Germain Bayon [c], Matthias Forwick [b], Christoph Vogt [d], Seung-Il Nam [a,*]

[a] Korea Polar Research Institute, Incheon 21990, Republic of Korea
[b] UiT The Arctic University of Norway, Department of Geosciences, NO-9037 Tromsø, Norway
[c] IFREMER, Marine Geosciences Unit, F-29280 Plouzané, France
[d] Crystallography, FB05 Geosciences & MARUM, University of Bremen, Klagenfurter Strasse 2-4, 28359 Bremen, Germany

ARTICLE INFO

ABSTRACT

The reconstruction of past ice sheet extents and dynamics in polar regions is essential for understanding the global climate system and obtaining more reliable predictions of future climate change. Here, we present a multi-proxy dataset integrating the Nd isotopic compositions (ε_{Nd}) of paired detrital and authigenic Fe oxide fractions, grain size distributions, organic geochemistry, and mineral assemblages in a glacimarine sediment core (core HH17–1085-GC) retrieved from the continental shelf off northern Svalbard. Our results indicate variability in sediment provenance and chemical weathering patterns since the last deglaciation, allowing us to distinguish a succession of distinct paleoclimate events: 1) a general retreat of the Svalbard-Barents Sea Ice Sheet (SBIS) from the continental shelf before ca. 16.3 ka BP; 2) an intense episode of meltwater discharge related to massive glacier loss between ca. 12.1–9.9 ka BP; and 3) a period of reduced meltwater input between ca. 9.9 and 2.7 ka BP followed by 4) a phase of glacier re-advance over the last two millennia. Evidence for the prolonged supply of radiogenic detrital ε_{Nd} and dolomite at the site of core HH17–1085-GC indicates that the onset of deglaciation offshore northeastern Svalbard may have occurred at least 1 ka later than that at the northwestern shelf, which can be further evaluated by obtaining a more precise end-member determination for the northeastern source with a quantitative ε_{Nd} dataset from Nordaustlandet. In the context where both polar sea-ice and oceanic circulation are expected to have played minor roles in determining the sedimentary ε_{Nd} compositions, the evidence for pronounced Nd isotopic decoupling between paired authigenic and detrital signatures ($\Delta\varepsilon_{Nd}$) at ca. 15.2 and 14.1 ka BP is interpreted as reflecting chemical weathering changes following the retreat of the SBIS on northern Svalbard, probably corresponding to punctual episodes of glacial re-advances. Our findings provide a better understanding of the deglacial history of northern Svalbard during and after the last deglaciation and highlight the utility of Nd isotopes as a proxy for reconstructing paleo-cryosphere changes.

1. Introduction

The Arctic Ocean has repeatedly undergone dramatic changes in the extent of ice coverage over glacial-interglacial cycles (review in Darby et al., 2006; Jakobsson et al., 2014; Stein, 2019). Since any change in the ice budget of polar regions exerts a strong influence on the global climate system through its impacts on ice albedo, freshwater removal/input to the ocean, and ocean circulation (e.g., Curry et al., 1995; Jang et al., 2013; Tarasov and Peltier, 2005), reconstructing the history of ice coverage within and around the Arctic Ocean can provide critical insights into our understanding of past, present, and future climate change. Svalbard is a key location for investigating past climate changes in the Arctic because this archipelago has been affected by various ice types during multiple glacial-interglacial cycles, including ice sheets, glaciers, and sea-ice. The general contour and extent of the Svalbard-Barents Sea Ice Sheet (SBIS) and glaciers on Svalbard during and after the Late Weichselian have been discussed for several decades (for the glaciers from Fjeldskaar et al., 2018 and references therein; for the ice

sheet from Hughes et al., 2016 and references therein). However, most of these earlier studies focused predominantly on western Svalbard (e.g., Ebbesen et al., 2007; Elverhøi et al., 1995; Svendsen et al., 1996).

Previous inferences of the glacial activity on the continental shelf off northern Svalbard have been based primarily on the occurrence of ice-rafted debris (IRD) and microfossils (e.g., core NP94–51 from Jernas et al., 2013; Koç et al., 2002; Ślubowska et al., 2005). Additionally, the ratio of neodymium (Nd) isotopes ($^{143}Nd/^{144}Nd$), expressed using the epsilon notation $\varepsilon_{Nd} = [(^{143}Nd/^{144}Nd)_{sample}/(^{143}Nd/^{144}Nd)_{CHUR}-1] \times 10^4$, where $(^{143}Nd/^{144}Nd)_{CHUR}$ is 0.512638 (Jacobsen and Wasserburg, 1980), is a powerful proxy in paleoclimate studies (Goldstein and Hemming, 2003; Jang et al., 2020). However, this tracer has yet to be applied for the reconstruction of past glacial activity offshore northern Svalbard. The ε_{Nd} signatures of the detrital fractions of marine sediments are inherited from their source rocks on continents, and hence their variation in sedimentary records can be used to track past changes in sediment provenance (e.g., Grousset et al., 1988; Horikawa et al., 2015; Jang et al., 2017; Revel et al., 1996). In glacimarine environments around Svalbard, sediment delivery is primarily related to the advance and retreat of ice sheets and/or glaciers in nearby drainage systems such that inferred provenance changes based on detrital ε_{Nd} can offer key information on the history of ice coverage patterns (e.g., Horikawa et al., 2015; Pereira et al., 2020). Recently, Jang et al. (2020) showed that the ε_{Nd} difference between the detrital and leached Fe oxide fractions from fjord sediments ($\Delta\varepsilon_{Nd}$) could also provide information on past glacier fluctuations. This new approach is based on the evidence that intense incongruent weathering of freshly exposed silicate rock substrates occurs during periods of glacier advance, resulting in enhanced Nd isotopic decoupling (i.e., higher $\Delta\varepsilon_{Nd}$ differences) (Jang et al., 2020). The use of Nd isotopes in both detrital and leached Fe oxide fractions of fjord sediments can thus provide useful information about the extent of ice sheets and glaciers in Arctic regions.

This paper presents Nd isotope ratios measured from the detrital and authigenic Fe oxide fractions of glacimarine sediments retrieved from the continental shelf off northern Svalbard to reconstruct the glacial history of the northern parts of the archipelago over the last 16.3 ka. Detrital ε_{Nd} records are supplemented and integrated with information about sediment structure, grain size, mineral assemblage, and organic geochemistry to reconstruct past changes in sediment provenance. Additionally, the ε_{Nd} difference between paired authigenic Fe oxide and detrital fractions ($\Delta\varepsilon_{Nd}$) is used as a proxy for glacial weathering to identify past periods of ice sheet instability and/or glacier fluctuation.
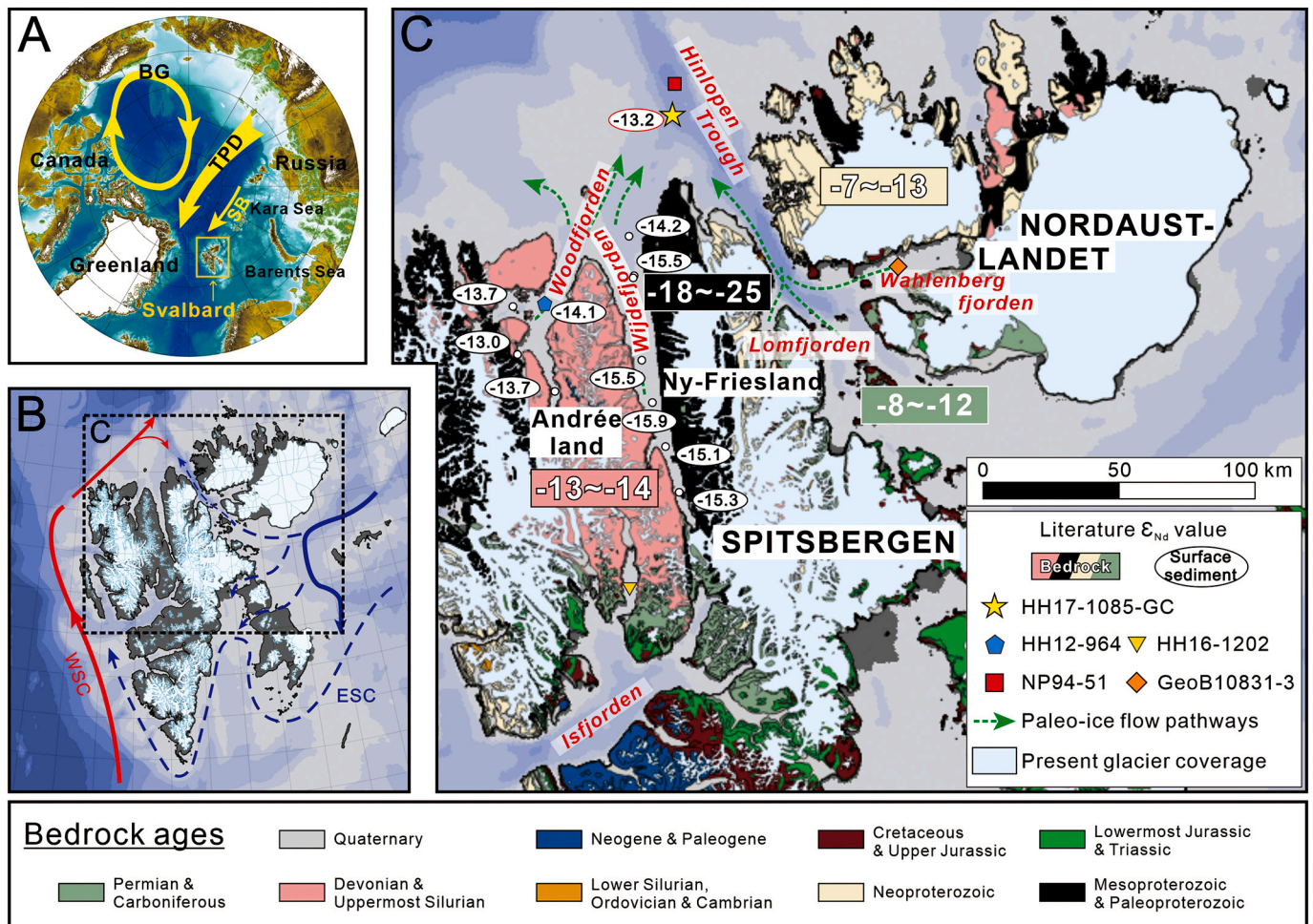

Fig. 1. (A) Map of the Arctic. The location of Svalbard is marked with the yellow rectangle, and water circulation patterns including the Beaufort Gyre (BG), Transpolar Drift (TPD) and Siberian Branch (SB) are indicated by yellow arrows. (B) Map of the Svalbard archipelago and surrounding waters. The West Spitsbergen Current (WSC) and the East Spitsbergen Current (ESC) are marked with red and blue arrows, respectively. (C) Map of northern Svalbard. The sampling site of core HH17–1085-GC and comparative sites of HH12–964, HH16–1202, NP94–51 and GeoB10831–3 are indicated. The Nd isotopic compositions (ε_{Nd}) of detrital or bulk fractions in bedrock (rectangles) and surface sediments (ellipses) near sampling site of core HH17–1085 (yellow star) are shown (data from Jang et al., 2020; Johansson et al., 1995, 2000, 2002; Johansson and Gee, 1999). Various bedrock ages are indicated by different colors. The proposed pathways of ice streams and sediment delivery in northern Svalbard are indicated by green dashed arrows (Batchelor et al., 2011; Dowdeswell et al., 2010), and present areas of glacier coverage are colored sky blue. (For interpretation of the references to colour in this figure legend, the reader is referred to the web version of this article.)

2. Physiographic setting

The Svalbard archipelago is located between 74 and 81°N and 10 and 35°E (Fig. 1A). It includes nine main islands, with Spitsbergen being the largest. Two different water masses bathe northern Svalbard: 1) the warm Atlantic Water (AW) carried by the Svalbard branch of the West Spitsbergen Current (WSC) and 2) the cold Arctic Water (ArW) carried by the East Spitsbergen Current (ESC) (Fig. 1B). Glacial troughs (~400 m deep) and shallower banks (Ottesen et al., 2007) characterize the continental shelf offshore northern Svalbard. This study focuses on the area offshore northern Spitsbergen where the trough continuing from Wijdefjorden and Hinlopen Trough merge.

There were several ice types on the archipelago during the Late Quaternary, including ice sheets, glaciers, and sea-ice in various configurations and extents. For example, during glacial periods this area was affected by glaciers/ice streams draining the SBIS (Ottesen et al., 2007). Sea-ice formation also occurs locally on Svalbard (Allaart et al., 2020; Bartels et al., 2017; Berben et al., 2017), and it can be transported to the area from the Arctic shelves via the Siberian Branch of the Transpolar Drift (TPD) (Tütken et al., 2002; Werner et al., 2014) (Fig. 1A). The Hinlopen Trough currently represents the main passage for the two main water masses in the area: 1) the southward inflow of the WSC and 2) the northward outflow of the ESC (Menze et al., 2019). However, during the Late Weichselian, it also acted as a major pathway for ice flow and sediment delivery (Batchelor et al., 2011) (Fig. 1C).

Based on the geological setting and regional ocean circulation patterns, the main source areas of terrigenous sediments deposited at the core site include Wijdefjorden and Woodfjorden on Spitsbergen and Nordaustlandet. Wijdefjorden is the longest fjord system on Svalbard. It separates Andrée Land to the west, where the outcrops comprise sedimentary rocks, including Devonian Old Red Sandstones, and Ny-Friesland to the east, where the outcrops comprise mainly Proterozoic metamorphic basement rocks (Dallmann, 2015; Hjelle, 1993) (Fig. 1C). In Woodfjorden, the bedrock geology is dominated by the Devonian Old Red Sandstone, with a minor contribution of Quaternary volcanic and Proterozoic rocks (Dallmann, 2015; Hjelle, 1993). In Nordaustlandet, Neoproterozoic and Permian to Carboniferous rocks are the main source rocks (Fig. 1C). The sediments deposited on the Arctic shelves can be further redistributed by sea-ice drifting as observed in the Fram Strait (Maccali et al., 2013; Tütken et al., 2002; Werner et al., 2014). Potential source regions include all areas surrounding the Arctic Ocean (i.e., the western and eastern Arctic) (Maccali et al., 2013). However, in the eastern Fram Strait, sediment sources are mostly restricted to the Eurasian shelf sediments (Tütken et al., 2002; Werner et al., 2014), in particular, the Kara Sea shelf (Pfirman et al., 1997; Werner et al., 2014), which presumably reflect the Siberian Branch-dominated water circulation pattern in the east. Given the position of our core site, located further eastward of eastern Fram Strait (Fig. 1), we consider exclusively the Kara Sea shelf sediments as a potential end-member of sea-ice-derived sediments from the Arctic Ocean.

3. Glacial history

According to the time-slice reconstruction of past Eurasian ice sheets (Hughes et al., 2016; Patton et al., 2017; Patton et al., 2016; Svendsen et al., 2004), Svalbard, apart from some nunataks (e.g., Landvik et al., 1998) was entirely covered by the SBIS extending to the continental shelf edges north and west of the archipelago during the Late Weichselian. The deglaciation from the shelf edges started ca. 19 ka BP (Jessen et al., 2010). A period of comparatively slow retreat between ca. 17 and 16 ka BP was followed by a more rapid ice sheet retreat towards the western and northern coasts of Svalbard at ca. 15 ka BP (Elverhøi et al., 1995; Landvik et al., 1998; Svendsen et al., 1992). The ice front reached the mouth of Wijdefjorden before ca. 14.5 ka BP (Allaart et al., 2020). The outer fjords of Svalbard were mostly ice-free after ca. 12 ka BP (Farnsworth et al., 2020; Hughes et al., 2016). In the inner fjords, the

timing of the deglaciation varied depending on the location. For example, the deglaciation terminated in Isfjorden at approximately 11.2 ka BP (Baeten et al., 2010; Elverhøi et al., 1995; Forwick and Vorren, 2009) and in Wijdefjorden at approximately 7.2 ka BP (Allaart et al., 2020; Braun, 2019).

The glacial coverage on Svalbard at ca. 10 ka BP remains controversial, with some models suggesting fully deglaciated conditions (e.g., the minimum and most-credible glacial scenario of Hughes et al., 2016) and others suggesting present-day glacier limits (e.g., the maximum glacial scenario of Hughes et al., 2016). While a recent modeling study supports the latter scenario based on sea-level observations (Fjeldskaar et al., 2018), a recently published data compilation suggests an intermediate glacial coverage between the aforementioned scenarios (Farnsworth et al., 2020).

During the early Holocene, the glacial coverage decreased, reaching a minimum extent at the beginning of the middle Holocene (ca. 8.0–6.0 ka BP; Farnsworth et al., 2020; Fjeldskaar et al., 2018). Massive glaciers on Svalbard, such as the ice caps on Nordaustlandet and in eastern Spitsbergen, survived the Holocene Thermal Optimum (ca. 11.2–5.2 ka BP), whereas smaller glaciers had mostly vanished by ca. 7.5–5.5 ka BP (Fjeldskaar et al., 2018). Subsequently, the glaciers began to grow or reform, as recorded in glacimarine and lake sediments (Baeten et al., 2010; Forwick et al., 2010; Røthe et al., 2015; Svendsen and Mangerud, 1997; van der Bilt et al., 2015), and reached their maximum post-glacial extents at various times during the late Holocene (Dowdeswell et al., 2020; Kempf et al., 2013; Martín-Moreno et al., 2017).

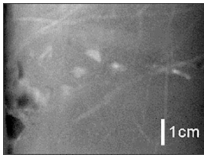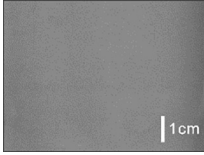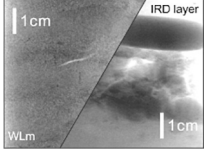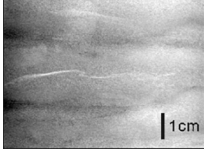## 4. Materials and methods

4.1. Sample collection

Sediment gravity core HH17–1085-GC (hereafter referred to as 1085-GC) (80.274°N, 16.211°E, ~322 m water depth; 462 cm long) provides the basis for this study. It was retrieved from the continental shelf off northern Spitsbergen during the 2nd Korea-Norway joint cruise of *RV Helmer Hanssen* (UiT The Arctic University of Norway) in 2017 (Fig. 1). The core site is located at the merger of a trough continuing as an extension of Wijdefjorden and the Hinlopen Trough. The temperature ($T \sim 1.6\,°C$) and salinity ($S \sim 34.77$ psu) of the bottom water at the site of 1085-GC differ slightly from those of the AW, characterized by $T > 3.0\,°C$ and $S > 34.65$ psu (Cottier et al., 2005), probably due to the mixing of the AW with the ArW transported by the ESC ($-1.5 < T < -1.0$ and $34.30 < S < 34.80$) (Cottier et al., 2005).

Braun (2019) performed laboratory work at UiT to determine the physical properties of the core and to acquire line-scan images and x-radiographs of the core (Table 1 and Fig. 2). Briefly, the wet bulk density and magnetic susceptibility of the whole core were determined at 1 cm intervals using a GEOTEK Multi-Sensor Core Logger (MSCL). The x-radiographs and line-scan images of the split cores were acquired using the GEOTEK MSCL-XCT X-ray imaging machine and the Avaatech XRF core scanner, respectively. The darker intervals on the x-radiographs indicate denser materials.

4.2. Grain size analysis

The grain size distributions were measured at 5 cm intervals using a laser diffraction instrument (Mastersizer 3000, Malvern) at the Korea Polar Research Institute (KOPRI). Before measurement, each sample was freeze-dried and then treated with 35% hydrogen peroxide to remove organic matter. Coarse grains larger than 1 mm (hereafter referred to as IRD) were counted at 1 cm intervals from x-radiograph images by Braun (2019). The mean sizes were calculated with GRADISTAT v 8.0 (Blott and Pye, 2001) using the method of Folk and Ward (1957).

Table 1

Summary of sedimentary facies in core HH17–1085-GC.

Unit	Facies/core depth	X-radiograph	Description	Depositional process
B2	Bioturbated sandy mud (Bsm) 30–0 cm		Dark grayish brown; sandy mud with some IRD (> 1 mm); poorly sorted; intensely bioturbated	Hemipelagic settling affected by drifting ice (sea-ice)
B1	Massive mud (Mm) 228–30 cm		Dark grayish brown; silt-rich massive mud, upward coarsening, IRD rare; poorly sorted; no primary structure, homogenous; a pale brown clay-rich layer at the base of this unit	Suspension plumes from meltwater plumes in ice-distal environment
A2	Weakly laminated mud (WLm) 385–228 cm		Mostly dark grayish brown; relatively silt-rich; poorly sorted; lamination blurred and more poorly defined upward in the core; an IRD-rich coarse layer between 360 and 370 cm (right part of figure)	Suspension settling from meltwater plumes in transitional environments from ice-proximal to ice-distal
A1	Laminated mud (Lm) 462–385 cm		Alteration between dark reddish gray and dark grayish brown; silt-rich and clay-rich muds without IRD; very poorly sorted; distinct and well laminated with good lateral continuity, lamination subparallel to slightly wavy	Suspension settling from meltwater plumes in ice-proximal environment.

4.3. AMS ^{14}C age dating

The age model for core 1085-GC is based on the integration of results from Braun (2019) and additional AMS ^{14}C analyses using the MICADAS system at the Alfred Wegner Institute – Helmholtz Centre for Polar and Marine Research (Table 2 and Fig. 3). The AMS ^{14}C ages were converted into calendar ages by applying the Marine13 dataset of the Calib Rev. 7.0.4 program (Stuiver and Reimer, 1993) with $\Delta R = 105 \pm 24$ yr for all samples (Mangerud et al., 2006). After rejecting four ^{14}C ages (Table 2; for details, see section 5.2), the age-depth model was determined with Bayesian age-depth modeling in BACON (v. 2.2; Blaauw and Christen, 2011) using R (v. 4.0.0; R Core Team 2020). We employed the default settings except for Student's t-distribution parameters t.a and t.b. The adjustments of those parameters (from t.a = 3 and t.b = 4 to t.a = 33 and t.b = 34) allowed the most recent age control point to be included in the age-depth model with a less smoothed age-depth relationship.

4.4. Bulk mineral assemblage analysis

X-ray diffraction pattern analyses were conducted at the University of Bremen. Dried bulk samples were grounded to a fine powder (<20 μm particle size) and prepared with the Philips backloading system. The X-ray diffractograms were measured on a Philips X'Pert Pro multipurpose diffractometer equipped with a Cu-tube (kα 1.541, 45 kV, and 40 mA), a fixed divergence slit of ¼°, a 16-sample changer, a secondary Ni filter, and the X'Celerator detector system. The measurements were performed as a continuous scan from 3 to 85° 2θ, with a calculated step size of 0.016° 2θ (the calculated time per step was 50 s). Mineral identification was achieved using the Philips software X'Pert HighScore™, and the identification of sheet silicates was performed with the software MacDiff 4.25 (Petschick et al., 1996). This was followed by a full quantification of the main mineral assemblages of the bulk fraction via the QUAX full pattern method (c.f., Vogt et al., 2002). A thorough preparation commonly increases the reproducibility of the results; however, the standard deviation given by Moore and Reynolds Jr (1989) of ±5% can be considered a general guideline for mineral groups with >20% clay fraction. The determination of major none clay minerals can be achieved with better standard deviations (± 1–3%; Vogt et al., 2002).

4.5. TOC, N_{org}, and $\delta^{13}C_{org}$ measurements

The contents of total organic carbon (TOC) and nitrogen (N_{org}) and the isotopic ratios of organic carbon ($\delta^{13}C_{org}$) were determined using an elemental analyzer (Flash 2000, Thermo Scientific) connected to an isotope ratio mass spectrometer (Delta V, Thermo Scientific) using continuous flow at KOPRI. For the determination of TOC and $\delta^{13}C_{org}$, the bulk sediments were powdered and then treated with 2 M hydrochloric acid for 24 h to eliminate inorganic carbonate. After sufficient rinsing with Milli-Q water (Millipore, >18.2 MΩ cm) and freeze-drying, the TOC contents and $\delta^{13}C_{org}$ were measured. The $\delta^{13}C_{org}$ of each sample is reported in per mil notation relative to the Vienna Pee Dee Belemnite international standard. The analytical precision is within 0.2‰. For the determination of N_{org}, we applied a KOBr-KOH solution to the powdered bulk sediments for separating inorganic and organic fractions of nitrogen (Silva and Bremner, 1966).

4.6. Neodymium isotopes analysis

Neodymium isotopic compositions of the authigenic (Fe-oxide rich) and detrital fractions of sediments were determined using a thermal ionization mass spectrometer (TIMS, Triton, Thermo Scientific) at KOPRI. The definitions of authigenic and detrital fractions follow those used by Jang et al. (2020). The authigenic fraction was obtained by leaching the bulk sediment using 0.02 M hydroxylamine hydrochloride in 25% acetic acid (hereafter, HH solution) at a 1:1 ratio of reagent and sediments for less than 1 h. Following the complete removal of any carbonate and authigenic fractions via exposure to the HH solution for more than 24 h (with a 10:1 ratio of reagent and sediment), the residual detrital fraction, mostly corresponding to the silicate-rich terrigenous material, was isolated. Detrital fractions were then digested using the alkaline fusion method described in Bayon et al. (2009), which ensured the complete dissolution of the silicate minerals.

Each fraction was purified by column chromatography using the combination of both TRU (100 μm, Eichrom) and Ln resins (100 μm, Eichrom) following a procedure modified from Pin and Zalduegui (1997). The neodymium isotope ratios were measured using TIMS and then normalized to the ^{144}Nd/^{146}Nd value of 0.7219 to correct for mass
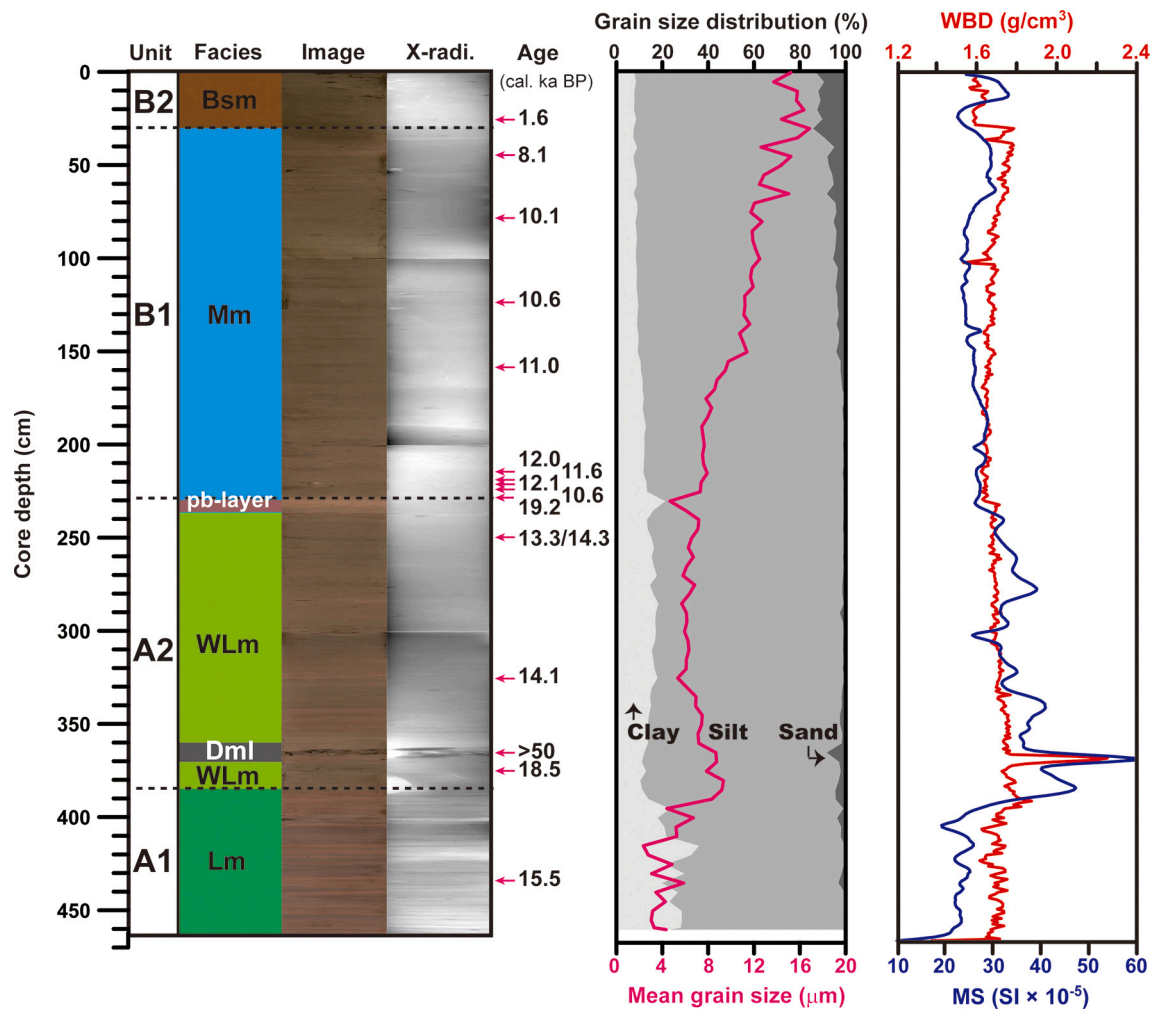
Fig. 2. Lithostratigraphic units and facies of core HH17–1085-GC based on line scan images and x-radiographs and grain size distribution, mean grain size, wet bulk density (WBD) and magnetic susceptibility (MS). BSM: bioturbated sandy mud; Mm: massive mud; pb-layer: pale-brown layer; WLm: weakly laminated mud; Dml: diamicton with lamination; Lm: laminated mud. The calibrated ^{14}C ages are indicated. For details, see Table 1. (For interpretation of the references to colour in this figure legend, the reader is referred to the web version of this article.)

Table 2
AMS ^{14}C ages and converted calendar ages of core HH17–1085-GC.

Lab ID	Unit	Core depth (cm)	AMS ^{14}C age (yr BP)	Cal. age (yr BP)	Material dated	References
Beta-529788	B2	25.5	2110 ± 30	1569 ± 63	Mollusk	This study
AWI 5473.1.1	B1	44.5	7694 ± 82	8053 ± 182	Mixed foram.	This study
AWI 5474.1.1	B1	79.5	9386 ± 92	10,082 ± 315	Mixed foram.	This study
Beta-529789	B1	122.5	9780 ± 30	10,573 ± 62	Mollusk	This study
AWI 5475.1.1	B1	159.5	10,168 ± 97	11,046 ± 279	Mixed foram.	This study
AWI 5476.1.1	B1	214.5	10,738 ± 103[a]	11,957 ± 520	Mixed foram.	This study
Beta-546258	B1	219.5	10,570 ± 30	11,606 ± 132	Mollusk	This study
AWI 2740.1.1	B1	221.5	10,829 ± 39[a]	12,143 ± 141	Mollusk	Braun (2019)
AWI 5103.1.1	B1	224.5	9827 ± 100	10,627 ± 216	Mixed foram.	This study
AWI 5104.1.1	A2	229.5[b]	16,492 ± 158[a]	19,282 ± 269	Mixed foram.	This study
AWI 5477.1.1	A2	249.5	11,885 ± 107	13,253 ± 241	Mixed foram.	This study
AWI 5478.1.1	A2	249.5[c]	12,794 ± 155[a]	14,344 ± 484	Mollusk	This study
AWI 2742.1.1	A2	326	12,696 ± 40	14,076 ± 80	Mollusk	Braun (2019)
Beta-509927	A2	365[b]	>43,500[a]	>50,000	Mollusk	This study
AWI 5105.1.1	A2	374.5[b]	15,745 ± 147[a]	18,491 ± 204	Mixed foram.	This study
AWI 5106.1.1	A1	434.5	13,479 ± 125	15,513 ± 263	Mollusk	This study

[a] Age inversion compared to below sampling depth.
[b] Discarded due to significant age inversion compared to below sampling depth.
[c] Discarded due to significant age inversion compared to the measurement from different material at the same sampling depth.
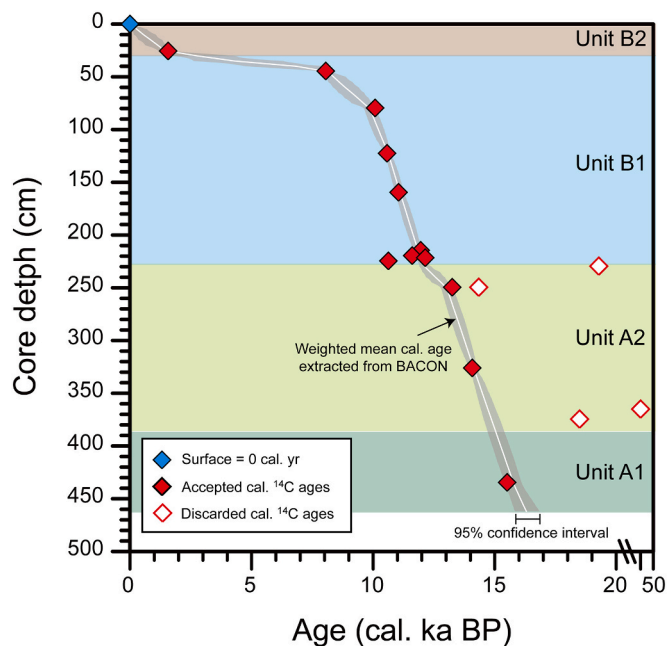
Fig. 3. Age model for core HH17–1085. Twelve ^{14}C ages were included (red diamonds) in the BACON model to determine the age-depth relationship (white line, weighted mean age). Four inverted ages were discarded (open diamonds). (For interpretation of the references to colour in this figure legend, the reader is referred to the web version of this article.)

fractionation. Long-term replicate analyses of the JNdi-1 reference solution (0.512110 ± 0.000014, $n = 12$) agreed well within uncertainty with the reference value of Tanaka et al. (2000), yielding an inferred external reproducibility of 0.3 ε_{Nd} units on measured Nd isotopic compositions. Note that the latter value was systematically taken for estimating the analytical uncertainty associated with studied samples unless the internal error during analysis was larger. The measurements of the BHVO-1 certified reference material (0.512972 ± 0.000011, $n = 3$) were also identical to the literature values within error (e.g., Raczek et al., 2003), confirming the accuracy of the Nd isotopic measurements performed in this study.

5. Results

5.1. Lithostratigraphy

Based on the sediment colour, texture, and structure, as well as its physical properties (wet bulk density and magnetic susceptibility), Braun (2019) defined two main lithostratigraphic units in core 1085-GC: a laminated unit from the core base to 228 cm and a massive unit above 228 cm. We name these units as unit A (lower) and unit B (upper) and further sub-divide them depending on their degree of lamination in unit A and bioturbation in unit B (Table 1 and Fig. 2). Lithostratigraphic unit A1, occurring from the bottom of the core to 385 cm, primarily consists of silt-rich and clay-rich mud (mean size: 2.3 to 8.3 μm; Supplementary Table S1). It has distinct laminations with cyclic alternation of dark reddish-gray (5YR 4/2) and dark-grayish brown layers (10YR 4/2). In this unit, the maximum IRD flux (> 1 mm) is 5 grains/cm^2·ka (Fig. 4), and biogenic detritus is sparse. The overlying unit A2, from 385 to 228 cm, is generally similar to unit A1 but comprises darker (2.5YR 4/2) and coarser sediments (4.7 to 9.3 μm; Supplementary Table S1). The lamination of this unit is blurred and more poorly defined upwards in the core. A very poorly sorted IRD-rich layer is intercalated in the lower part of unit A2 (360–370 cm) (Table 1 and Fig. 2), and a distinct pale-brown layer (7.5YR 4/2) is identified at the top of this unit (228–238 cm). In the IRD-rich layer, IRD flux (> 1 mm) exceeds 24 grains/cm^2·ka. Stratigraphic unit B1 is defined as the depth interval between 228 and 30 cm and is composed of massive (dark grayish brown 10YR 4/2 to weak red 2.5YR 4/2) silt-rich mud (7.3 to 15.8 μm; Supplementary Table S1). There is a coarsening upward trend (Fig. 2), and bioturbation is generally absent. The top-most unit, B2, is above 30 cm depth and is composed of IRD-rich (Fig. 4), dark grayish-brown (2.5YR 4/2) sandy mud sediments (13.7 to 16.8 μm; Supplementary Table S1). The interval is intensely bioturbated.

5.2. Chronostratigraphy and sediment accumulation rate

The AMS ^{14}C ages and converted calendar ages are listed in Table 2. The youngest age was detected at the shallowest depth of 25.5 cm (ca. 1.6 ka BP), while the oldest age was determined at a depth of 365 cm (> 50 ka BP), where massive clasts up to ~2 cm occur (Fig. 3). The dating results revealed six ages that were inverted relative to the ages of the corresponding sampled depths below throughout the core; three
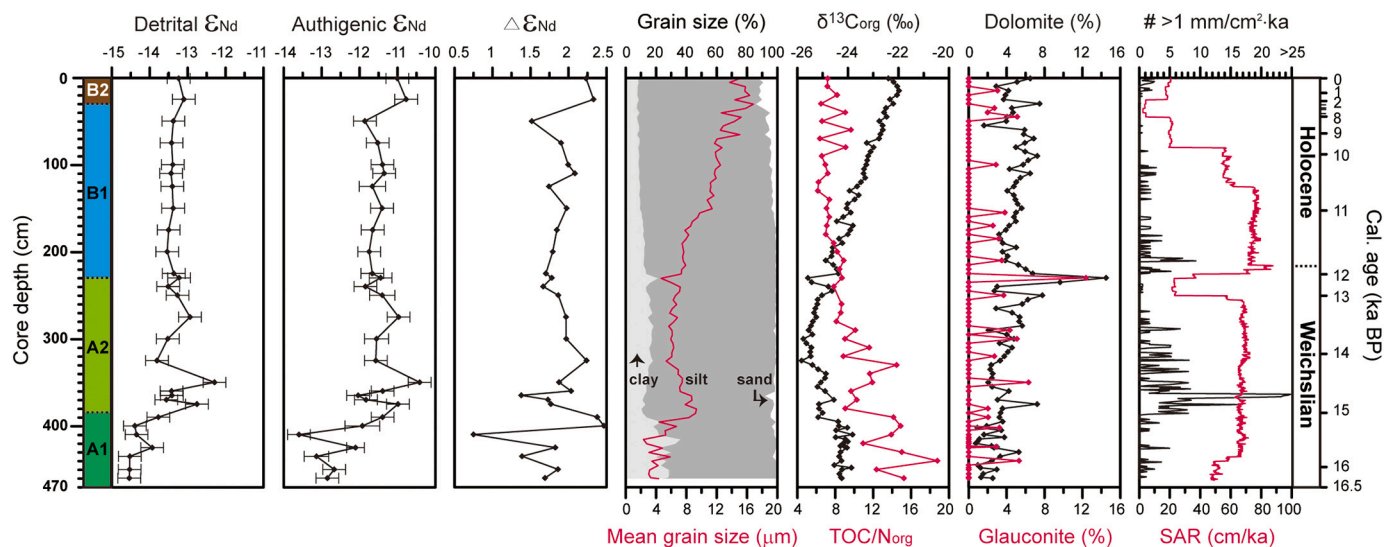

Fig. 4. Geochemical proxies, including detrital and authigenic ε_{Nd}, $\Delta\varepsilon_{Nd}$, grain size distribution, mean grain size, $\delta^{13}C_{org}$, TOC/N$_{org}$, the contents of dolomite and glauconite, calculated IRD (> 1 mm) flux and sediment accumulation rate (SAR) in core HH17–1085-GC. Error bars for ε_{Nd} represent $\pm 2\sigma$ uncertainties. (For interpretation of the references to colour in this figure legend, the reader is referred to the web version of this article.)

represented significant age inversions and were therefore excluded from the determination of the age-depth model (Table 2). Different materials were used for dating at ~249.5 cm. They revealed a relatively older age for mollusk shell fragments (ca. 14.3 ka BP) than for corresponding assemblages of mixed benthic foraminifera (ca. 13.2 ka BP); thus, the older age was discarded.

The weighted mean values extracted by BACON indicate that the bottom age of core 1085-GC is ca. 16.3 ka BP, and the average sediment accumulation rate was ~28.3 cm/ka (Figs. 3 and 4). This rate is lower than that of core NP94–51, from a nearby site (~42.0 cm/ka; Ślubowska et al., 2005). According to the age model, units A1 and A2 were deposited between ca. 16.3 and 12.1 ka BP, whereas units B1 and B2 were deposited from ca. 12.1 ka BP to the present. The sediment accumulation rate was generally higher between ca. 15.8 and 10.5 ka BP, with a marked decrease observed between ca. 13.0 and 12.1 ka BP. There was a stepwise decrease in the sediment accumulation rate after ca. 9.8 ka BP until ca. 5.3 ka BP, when an overall minimum was reached (Fig. 4)(Allaart et al., 2020).

5.3. Dolomite and glauconite contents

The dolomite content ranges from 0.7 to 14.5%, with an average value of 4.2% (1σ, n = 99) (Supplementary Table S1 and Fig. 4). The abundance of dolomite is generally lower within unit A1 (average of 2.3 ± 1.2%, 1σ, n = 22) than in the other units, whereas its variability is largest within unit A2 (average of 4.5 ± 2.6%, 1σ, n = 31) (Fig. 5). A prominent dolomite peak up to 14.5% occurs in the pale brown layer in the uppermost part of unit A2. This peak corresponds to an abrupt increase in glauconite content to 12.4%, which is almost 15 times higher than the average glauconite content across the entire core (0.8 ± 1.9%, 1σ, n = 31) (Fig. 4).

5.4. TOC, N_{org} and $\delta^{13}C_{org}$

The overall ranges of TOC and N_{org} are 0.2–1.5% and 0.02–0.16%, respectively (Supplementary Table S1). These two parameters strongly correlate with each other (r = 0.93, n = 46) and generally have largely

Fig. 5. Box and whisker plots of dolomite contents, detrital and authigenic ε_{Nd}, and the ε_{Nd} differences ($\Delta\varepsilon_{Nd}$) within each lithological unit. Note that the exceptional outlier of dolomite within the pale-brown sediments in unit A2 was discarded for the calculation. (For interpretation of the references to colour in this figure legend, the reader is referred to the web version of this article.)

uniform values within units A1 and A2, gradually increasing towards the core-top within units B1 and B2. The TOC/N_{org} ratios are much lower within units B1 and B2 (7.5 ± 1.0, 1σ, n = 23) than within unit A1 (14.4 ± 2.3, 1σ, n = 8) (Fig. 4). The $\delta^{13}C_{org}$ values show a decreasing trend from the bottom (−24.2‰) to the middle of stratigraphic unit B1 (down to −25.8‰) and then a gradually increasing trend upward (up to −22.0‰) (Fig. 4).

5.5. Detrital and authigenic ε_{Nd}

The detrital and authigenic ε_{Nd} values of core 1085-GC range from −14.5 to −12.3 (−13.6 ± 0.5, 1σ, n = 29) and −13.6 to −10.4 (−11.7 ± 0.7, 1σ, n = 29), respectively, throughout the core (Supplementary Table S3 and Fig. 4). Both ε_{Nd} values are generally well correlated (r = 0.87, n = 29). Less radiogenic ε_{Nd} values characterize unit A1, with a minimum of −14.5 (−13.6) for the detrital (authigenic) components and a generally upward increasing trend (Fig. 5). In unit A2, the background ε_{Nd} values for detrital and authigenic components are ~ −13.8 and −12.0, respectively, but radiogenic ε_{Nd} peaks of −12.8 and −11.0, respectively, occur in this sediment interval in association with the presence of episodic IRD. In unit B1, the ε_{Nd} values of both components are relatively uniform without any particular fluctuation, showing mean values of −13.4 ± 0.1 for detrital (1σ, n = 9) and −11.6 ± 0.2 for authigenic (1σ, n = 9) components. In unit B2, the detrital and authigenic ε_{Nd} values are relatively high, up to −13.1 and −10.8, respectively, with larger variability in authigenic ε_{Nd}.

6. Discussion

6.1. Sediment provenance interpretation

Detrital ε_{Nd} values provide a powerful means for identifying any downcore variation in sediment provenance in our study areas, including Woodfjorden, Wijdefjorden, Nordaustlandet and the Kara Sea shelf. The ε_{Nd} values from the literature for outcrops in Woodfjorden, Wijdefjorden and Nordaustlandet and sea-ice rafted sediments on the Kara Sea shelf can be divided into four groups: 1) unradiogenic (low) ε_{Nd} values from eastern Wijdefjorden (−25.4 < ε_{Nd} < −18.6; Johansson et al., 1995; Johansson and Gee, 1999), 2) intermediate ε_{Nd} values from Woodfjorden and western Wijdefjorden (ε_{Nd} ~ −13.6 for the so-called Devonian Old Red Sandstone from Jang et al., 2020), 3) the most radiogenic (high) ε_{Nd} compositions from Nordaustlandet (−13.2 < ε_{Nd} < −7.4; Johansson et al., 2000; Johansson et al., 2002) and 4) the Kara Sea shelf (ε_{Nd} ~ −8.9; Tütken et al., 2002) (Fig. 1C). Note that the catchment area of Lomfjorden on northeastern Ny-Friesland is primarily dominated by Permian rocks (Blomeier et al., 2011), implying different ε_{Nd} values from those of eastern Wijdefjorden where Proterozoic to lower Silurian metamorphic rocks predominate (Dallmann, 2015) (Fig. 1C). We assume that this provenance is characterized by a relatively radiogenic ε_{Nd} based on the recent measurements of detrital ε_{Nd} from Permian rocks collected near Isfjorden and Kongsfjorden in Svalbard ranging from −11.6 to −8.5 (Jang et al., 2020) (Fig. 1C).

The sediment mineral assemblages represent an additional proxy for identifying sediment provenance, which complements the use of Nd isotopes. In this study, the presence of dolomite in the sediments can be unambiguously attributed to detrital inputs from dolostones outcropping in the Neoproterozoic basement on southwestern Nordaustlandet (Kunzmann et al., 2015) and/or from the Permian sedimentary sequence in northeastern Ny-Friesland (Blomeier et al., 2011). Detrital input from both sources would be likely to be accompanied by an increase in ε_{Nd}, although differing from other radiogenic but dolomite-poor sediment sources derived from, for instance, the Kara Sea shelf. On the basis that rises in detrital ε_{Nd} are generally associated with increases in dolomite (Figs. 4 and 5), we infer that the Kara Sea shelf does not represent a dominant source of sediment in the studied area. Considering the location of the two potential sources considered in this study
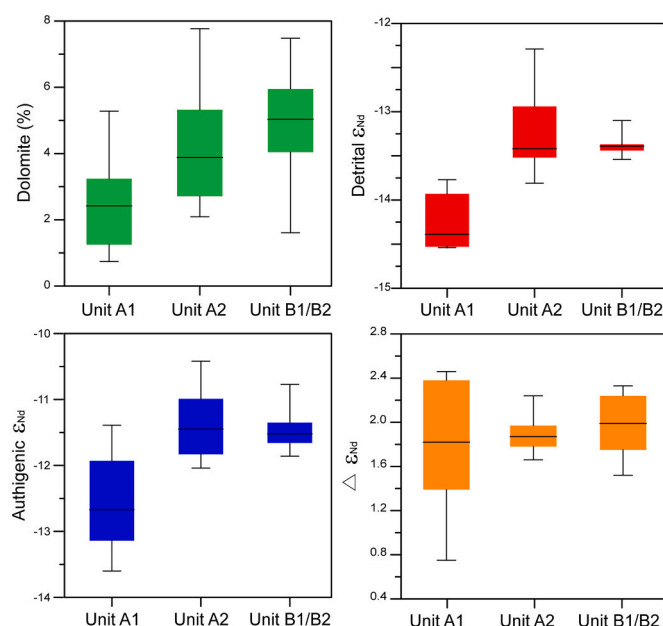
(Nordaustlandet and northeastern Ny-Friesland), together with water circulation patterns and past ice-flow directions (e.g., Batchelor et al., 2011; Dowdeswell et al., 2010; Hormes et al., 2011), the Hinlopen Strait represents the most plausible pathway for dolomite delivery to the core site. Therefore, we hereafter refer to both sources as 'the Hinlopen-source'. The supply of detrital sediments from the Hinlopen-source is supported by an increase in the detrital ε_{Nd} value of the surface sediments of up to 2.7 on the contiental shelf off northern Svalbard compared with those in inner Wijdefjorden (Jang et al., 2020) (Fig. 1).

Likewise, the presence of glauconite can be traced back to the terrestrial input from the Carboniferous and Permian sedimentary rocks in the Wahlenbergfjorden catchment area in southwestern Nordaustlandet where glauconite-rich beds are common (e.g., Bond et al., 2018; Lauritzen, 1981). Glauconite is also present in small amounts as streaks and patches within the dolomite sequence in northeastern Ny-Friesland (Fortey and Bruton, 1973), and thus this area could be a minor source.

6.2. Glacimarine sedimentary and environmental changes in northern Svalbard

6.2.1. Late Weichselian – early deglaciation (unit A1, 16.3–15.0 ka BP)

The lowermost unit, A1, characterized by fine-grained laminations, is suggested to have been deposited in an ice-proximal setting that prevailed between ca. 16.3 and 15.0 ka BP (hereafter referred to as the early deglaciation period) (Table 1 and Fig. 2). Fine-grained laminated glacimarine sediments in Svalbard fjords typically correspond to depositional environments associated with the settling of meltwater plume-derived suspended particles in ice-proximal environments (e.g., Elverhøi et al., 1995; Forwick and Vorren, 2009; Forwick et al., 2010). During the retreat of the ice margin (e.g., tidewater glaciers and/or ice sheets), the mixing of meltwater with ambient seawater initiates a buoyant plume from which the settling of suspended particles is size-dependent, generating laminated structures (review in Ó ÓCofaigh and Dowdeswell, 2001). In full agreement with this interpretation, we suggest that the sediment deposited during the early deglaciation period derived primarily from meltwater plumes emanating from the retreating marine-terminating margin of the ice sheet that existed on the contiental shelf off northern Svalbard. Our data indicate that the ice extent at approximately 16 ka BP was slightly smaller than that proposed by Hughes et al. (2016), who showed that the SBIS nearly covered Svalbard, including our core site, at ca. 16 ka BP (Fig. 6A) before retreating towards the mouth of Wijdefjorden and Woodfjorden during the early deglaciation. Light $\delta^{13}C_{org}$ values and high TOC/N$_{org}$ ratios indicate organic matter of predominantly terrestrial origins in Svalbard fjord sediments (Knies and Martinez, 2009; Winkelmann and Knies, 2005) (Fig. 4) most likely delivered via subglacial conduits at the base of the
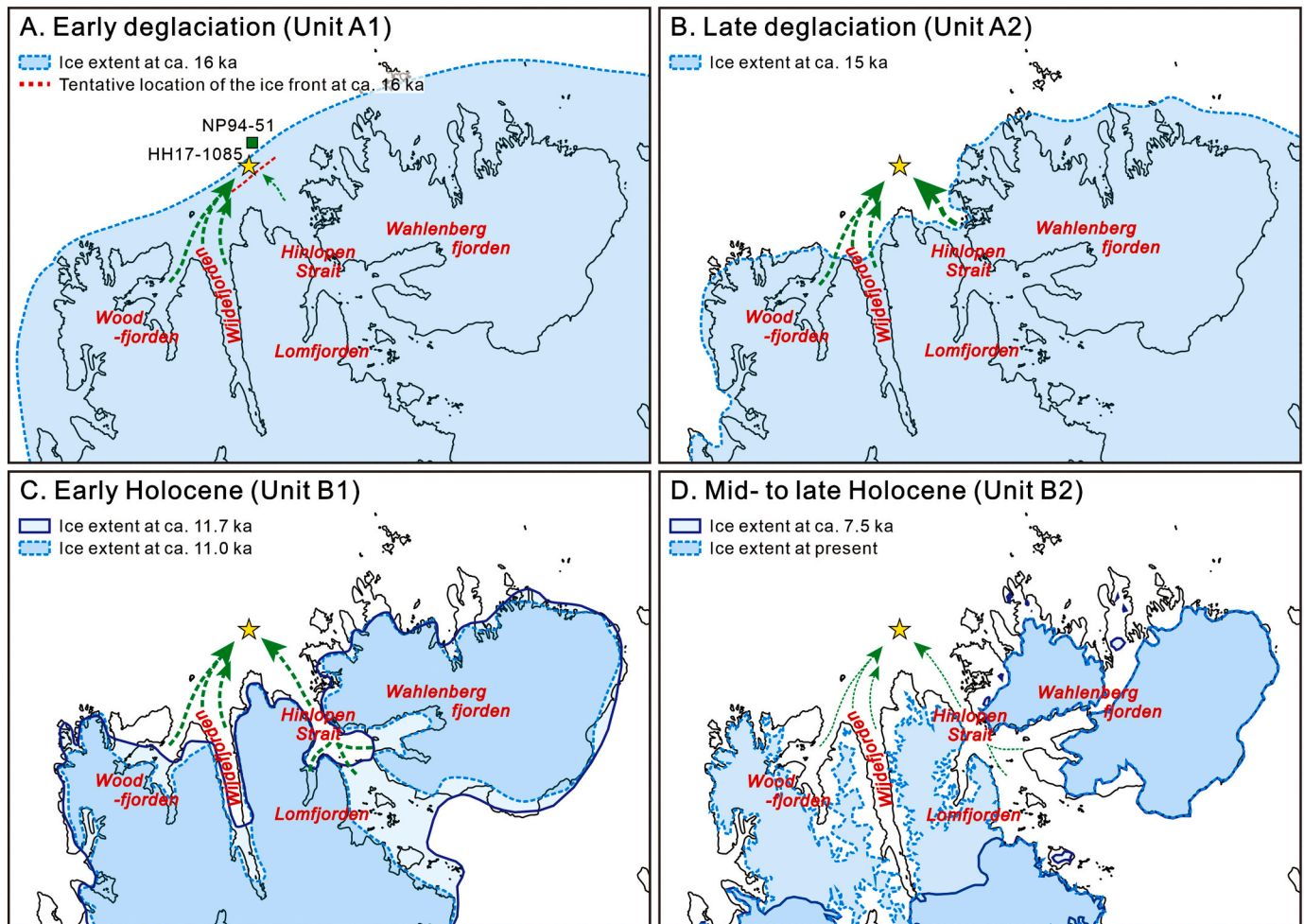

Fig. 6. Schematic illustrations of the potential pathways of sediments with estimated ice extents during (A) the early deglaciation, (B) the late deglaciation, (C) the early Holocene, and (D) the middle to late Holocene. The assumed pathways for sediment delivery are marked with green dashed arrows. The estimated extents of the Svalbard-Barents Sea Ice Sheet (SBIS) and land glaciers are generally consistent with previous reconstructions from the most credible DATED-1 timeslices (16 and 15 ka BP; Hughes et al., 2016), the SVALHOLA database (11.7 and 11.0 ka BP; Farnsworth et al., 2020), best-fit model (7.5 ka BP; Fjeldskaar et al., 2018) and satellite images (present; Nuth et al., 2013). However, our data indicate that the ice extent around 16 ka BP terminated further south (red dotted line in Fig. 6A) than suggested by Hughes et al. (2016). (For interpretation of the references to colour in this figure legend, the reader is referred to the web version of this article.)

SBIS. Such subglacial pathways could have transported land-derived material and re-mobilized glacimarine sediments to the adjacent ice margin.

In this study, our suite of provenance proxies suggests that the sediment deposited at the core location during the early deglaciation period was mostly derived from the Devonian Old Red Sandstone, which is dominant in the catchment areas of Woodfjorden and Andrée Land to the west of Wijdefjorden. The detrital ε_{Nd} values of the sediments (-14.3 ± 0.3, 1σ, $n = 7$) are slightly less radiogenic than those of the Devonian Old Red Sandstone (-13.6 ± 0.3 from Jang et al., 2020) but very similar to those for core-top sediments at the mouth of Wijdefjorden (-14.2 ± 0.2 from Jang et al., 2020) and central Woodfjorden (-14.1 ± 0.2 from Jang et al., 2020) (Fig. 1C). This origin is further supported by the overall reddish colour of the sediment, which is consistent with the Devonian Old Red Sandstone (Blomeier et al., 2003a; Blomeier et al., 2003b; Rasmussen and Thomsen, 2013). The mixing of detrital sediment sources from east Wijdefjorden and Nordaustlandet, characterized by less and more radiogenic ε_{Nd} signatures, respectively, could possibly account for the observed ε_{Nd} sediment signatures. However, the generally low dolomite contents in core 1085-GC sediments suggest that these sources only acted as minor sediment contributions during this period. Accordingly, we propose that the sediment supply was dominated by input from the western sources, probably reflecting enhanced deglaciation on northwestern Svalbard (Fig. 6A).

6.2.2. Late Weichselian – late deglaciation (unit A2, 15.0–12.1 ka BP)

The seesaw fluctuations in detrital ε_{Nd} values in the deposits between ca. 15.0 and 12.1 ka BP (hereafter referred to as the late deglaciation period) probably reflect the interplay between various sediment sources from Woodfjorden, Wijdefjorden, and Nordaustlandet (Fig. 4). In this context, less radiogenic ε_{Nd} values would reflect enhanced detrital contributions from Woodfjorden and Wijdefjorden, whereas more radiogenic ε_{Nd} values would presumably correspond to inputs from Nordaustlandet (Fig. 6B).

The most notable feature of unit A2 is the overall increase in sedimentary ε_{Nd} values (Fig. 4). Given the Nd isotopic compositions of the potential sources, the observed ε_{Nd} shift towards more radiogenic values can be attributed to enhanced terrestrial inputs from the Hinlopen-source, presumably via northward glacier drainage through the Hinlopen Strait (e.g., Batchelor et al., 2011; Dowdeswell et al., 2010) (Fig. 1). An accompanying increase in dolomite (Fig. 4) supports Nordaustlandet and northeastern Ny-Friesland as potential source regions (compare with Kunzmann et al., 2015). Enhanced sediment supply from the Hinlopen-source was accompanied by the episodic occurrence of IRD (Figs. 2 and 4), suggesting partial break-up of the SBIS on the northeastern margin of Svalbard at ca. 15.0 ka BP (Fig. 6B). Alternatively, the IRD-rich sediments overlying the laminated mud could be interpreted as reflecting the disappearance of sea-ice, which impacts iceberg drift (Kleiber et al., 2000; Ó ÓCofaigh and Dowdeswell, 2001). However, the observed lack of diatom species at the neighboring site represented by core NP94–51 suggests that sea-ice coverage was extensive at that time (Koç et al., 2002), which rules out this latter hypothesis. Therefore, the transition of the primary provenance from northwestern to northeastern Svalbard implies that the retreat of the SBIS on the northeastern margin of Svalbard started later than that at the northwestern margin. The delayed retreat of the SBIS at the northeastern margin of Svalbard may have been related to the strong subsurface intrusion of warm AW to northern Svalbard during that time (Ślubowska et al., 2005). However, this suggestion remains speculative for the time being and cannot be evaluated until additional quantitative ε_{Nd} data from Nordaustlandet become available.

The progressive disappearance of laminated sediment at the studied site after the partial break-up of the SBIS along the northeastern margin of Svalbard indicates a gradual transition from ice-proximal to ice-distal glacimarine environments (Ó ÓCofaigh and Dowdeswell, 2001). Upward decreases in the sand/mud and silt/clay ratios support a progressive increase in the distance between the retreating ice margin and the core location (e.g., Mackiewicz et al., 1984). This finding is consistent with previous studies that documented the ongoing retreat of the SBIS from the northern Svalbard coast into mid-Wijdefjorden, Woodfjorden, and the Hinlopen Strait during the late deglaciation period (Allaart et al., 2020; Bartels et al., 2017; Hughes et al., 2016 and references therein) (compare Fig. 6A with Fig. 6B).

The final phase of the deglaciation is marked by the deposition of a pale-brown sediment layer at ca. 12.1 ka, which corresponds to an abrupt increase in dolomite (~14.5%) and glauconite (~12.4%) contents at the top of A2 (Fig. 4). These changes in the sediment mineral assemblage indicate sediment input predominantly from the catchment area of Wahlenbergfjorden on southwestern Nordaustlandet with a minor contribution from northeastern Ny-Friesland (see *section 6.1*). Bartels et al. (2018) reported the occurrence of similar pale-brown sediment in the bottommost part of a core GeoB10831–3 retrieved from inner Wahlenbergfjorden (before ca. 11.3 ka BP) (Fig. 1C). Nevertheless, the detrital ε_{Nd} values at core 1085-GC (Fig. 4) are less radiogenic than the representative ε_{Nd} values of bedrock in western and central Nordaustlandet ($-13.2 < \varepsilon_{Nd} < -7.4$; Johansson et al., 2000; Johansson et al., 2002) and northeastern Ny-Friesland ($-11.6 < \varepsilon_{Nd} < -8.5$; Jang et al., 2020) (Fig. 1), which could be at least partly attributable to less radiogenic Nd inputs from northwestern detrital sources.

The deposition of such a homogenous layer of sediments delivered mainly from southwestern Nordaustlandet to the continental shelf off northern Svalbard could reflect either rapid retreat/collapse of glaciers, or increased meltwater release. The rapid retreat or collapse of glaciers can lead to the deposition of coarse-grained materials. However, the increase in clay content and absence of IRD in this layer suggest that this layer was caused by a meltwater pulse accompanied by considerable sediment transport rather than by deposition from ice rafting. This pulse could be attributed to a rapid transition from cold conditions during the Younger Dryas, 12.9–11.7 ka BP, to warm conditions (Farnsworth et al., 2020 and references therein). Considering the potential age uncertainty inferred from the younger ^{14}C ages above this layer (10.6 ka BP; Fig. 3), this distinct sediment layer might correspond to the second-largest meltwater pulse MWP-1B reconstructed in Storfjorden at 11.3–11.0 ka BP (e.g., Tian et al., 2020), implying ubiquitous glacier melting across Svalbard after the Younger Drays. However, there are several dates providing older ages from shallower core depths (12.1–11.6 ka BP; ~15 cm above; Fig. 3); thus, this meltwater pulse more likely reflects a local event.

6.2.3. Latest Weichselian – Holocene (units B1 & B2, 12.1 ka BP to the present)

Unit B1, characterized by the massive fine-grained mud, was deposited in a more distal glacimarine environment between ca. 12.1 and 2.7 ka BP (Allaart et al., 2020; Ó ÓCofaigh and Dowdeswell, 2001). In the lower part of unit B1, deposited between ca. 12.1 and 9.9 ka BP, the sediment accumulation rate remained considerably high (Fig. 3), suggesting high meltwater discharge during the early Holocene (Farnsworth et al., 2020) (Fig. 6C). Indeed, proxy records show that glaciers on Svalbard experienced massive losses during the early Holocene (Farnsworth et al., 2020, and references therein). This is in accordance with a recent modeling study based on relative sea-level showing the disappearance of all glaciers except for the largest glaciers in Nordaustlandet and eastern Spitsbergen before 7.5 ka BP (Fjeldskaar et al., 2018). This extensive melting of glaciers probably produced large meltwater runoff, resulting in relatively high sediment flux throughout the early Holocene, as recorded in Svalbard fjord sediment cores (Allaart et al., 2020; Bartels et al., 2018; Bartels et al., 2017; Flink et al., 2017; Hald et al., 2004) and at our core site off northern Svalbard.

The sediment accumulation rate decreased as the deglaciation proceeded through the middle Holocene (Fig. 4), when glaciers on Svalbard reached their Holocene minimum extent (Farnsworth et al., 2020)

(Fig. 6D). In particular, the upper part of unit B1 deposited between ca. 8.0 and 2.7 ka BP is characterized by the lowest sediment accumulation rates in our record, suggesting sediment deficiency, as has been ubiquitously documented for the middle Holocene in other Svalbard cores (e. g., Allaart et al., 2020; Bartels et al., 2017; Flink et al., 2017; Rasmussen and Thomsen, 2014). The reduced sediment accumulation rate at that time likely reflects the gradual reduction/disappearance of glaciers and, as a consequence, the reduced supply of terrestrial material, including fine-grained materials (Fig. 4). The possibility of reduced terrestrial input is indirectly supported by the increased contribution of marine organic matter to the total organic carbon budget at the site of core 1085-GC, as inferred from the high $\delta^{13}C_{org}$ and low TOC/N_{org} values (Fig. 4). On the other hand, the glaciers that re-advanced and/or survived during those times (Farnsworth et al., 2020; Fjeldskaar et al., 2018) could have contributed to an increase in sand content (Fig. 4). Such a sand increase would have been enhanced by the winnowing of bottom currents due to a shallowing of the water depth in response to post-glacial isostatic uplift (Forman et al., 2004).

The mean grain size and sand contents are highest in unit B2 deposited after ca. 2.7 ka BP, and the IRD flux in this unit is high (Fig. 4). These characteristics reflect glacier advances (e.g., Allaart et al., 2020) corresponding to the general cooling in Svalbard during this period (Dowdeswell et al., 2020; Forwick and Vorren, 2009; Hald et al., 2004; Svendsen and Mangerud, 1997). The high sand content during this interval is likely associated with ice-rafting processes. The advances of glaciers on northern Svalbard during the late Holocene would have led to intensified iceberg production (Allaart et al., 2020; Bartels et al., 2017; Ślubowska et al., 2005), delivering coarse-grained sediments to the continental shelf. Sea-ice rafting could have also contributed to the transport of coarse-grained sediments from the shore to the continental shelf. This interpretation is supported by the gradual increase in sea-ice cover at the mouth of Wijdefjorden during the last few millennia (Allaart et al., 2020) and the temporarily enhanced sea-ice cover at NP94–51 during the Little Ice Age (Jernas et al., 2013).

During the Holocene, the sediment provenance remained more constant than during the deglaciation, as evidenced by the near-constant detrital ε_{Nd} signatures. The detrital ε_{Nd} values are generally comparable to those encountered during the final phase of deglaciation, which suggests sediment supply from similar source regions. However, the occurrence of low-to-moderate dolomite and glauconite contents could indicate that reduced sedimentary inputs from southwestern Nordaustlandet contributed to the Hinlopen-source (Fig. 4); this reduced input was probably due to the increase in distance between the glacial source of the sediments and the core site as glaciers retreated.

6.3. Application of $\Delta\varepsilon_{Nd}$ as a proxy for reconstructing glacial activity in northern Svalbard

The Nd isotopic composition of authigenic Fe oxide fractions has been widely used as a proxy for water masses in paleoceanographic studies. The Nd isotopic variations in the leached Fe oxide fractions of marine sediment records can provide information on past hydrological changes, such as the strength of the Atlantic Meridional Overturning Circulation (e.g., Böhm et al., 2015; Jonkers et al., 2015; Piotrowski et al., 2005; Rutberg et al., 2000), dense water formation (e.g., Jang et al., 2017) and meltwater discharge events (e.g., Jang et al., 2013). Meanwile, recent studies have shown that weathering processes in catchments hosting sedimentary rocks (such as in Svalbard) could be accompanied by the release of dissolved Nd isotopic signatures (and associated Fe oxide phases) being significantly more radiogenic than the corresponding detrital sediment fraction (Bayon et al., 2020; Hindshaw et al., 2018; Jang et al., 2020). The application of this new ε_{Nd} approach to Svalbard fjord sediments showed that the analysis of paired detrital and authigenic fractions could provide useful information on the degree of incongruent chemical weathering and associated glacial evolution (e. g., Jang et al., 2020).

At the site of core 1085-GC, authigenic ε_{Nd} values are strongly correlated with corresponding detrital ε_{Nd} values ($r = 0.87$, $n = 29$) (Fig. 4), suggesting that the dissolved terrestrial input exerts a strong influence on the ε_{Nd} composition of leached Fe oxide phases. As proposed by Jang et al. (2020), this correlation in Svalbard fjord sediments suggests that meltwater releases are accompanied by substantial delivery of dissolved Fe and rare earth elements derived from the chemical weathering of rocks hosted in glaciated catchments, thereby leading to subsequent co-precipitation of abundant Fe oxide phases in the water column. Alternatively, the presence of ancient preformed Fe oxides delivered by meltwater discharge and sea-ice entrainment could also dominate the leached ε_{Nd} signal extracted from the studied fjord sediments (Bayon et al., 2004; Bayon et al., 2020; Werner et al., 2014). However, the authigenic ε_{Nd} values (from −13.6 to −11.4) obtained for the early deglaciation period are considerably less radiogenic than the ε_{Nd} value of leached (preformed) phases from the Devonian Old Red Sandstones (−10.8 from Jang et al., 2020), and those retrieved from Kara Sea shelf sediments (−4.2 from Chen et al., 2012; −5.9 from Haley and Polyak, 2013), suggesting that these latter sediment sources were not important sources of 'terrestrial' preformed Fe oxides in Svalbard fjords.

Since the strong correlation between detrital and authigenic ε_{Nd} values may be a coincidence, we evaluated the possibility that both ε_{Nd} signatures originate from separate sources. In the Fram Strait, the ε_{Nd} variability in sedimentary authigenic fractions has been interpreted as reflecting changes in the relative influence of AW (−13.2 to −13.0 from Teschner et al., 2016) and comparatively more radiogenic ArW (−9.9 from Laukert et al., 2017) (Maccali et al., 2013; Rahaman et al., 2020; Werner et al., 2014). On this basis, the radiogenic excursion for authigenic ε_{Nd} identified at the site of core 1085-GC during the late deglaciation period (ca. 15–14 ka BP) could possibly be explained by a stronger influence of the ArW offshore northern Svalbard. However, the increase in *C. neoteretis* at the neighboring site represented by core NP94–51 indicates a stronger inflow of relatively warm AW (Ślubowska et al., 2005), suggesting that the observed authigenic ε_{Nd} excursion towards radiogenic values cannot be interpreted as a re-organization of ocean circulation patterns. Furthermore, while the increase in authigenic ε_{Nd} observed at the studied site corresponding to the early stage of the late Holocene could be attributed partly to reduced inflow of the AW (Ślubowska-Woldengen et al., 2007; Ślubowska et al., 2005; Werner et al., 2014), this hypothesis disagrees with paleoceanographic reconstructions indicating the increased inflow of AW during the latter stage of the late Holocene (Rasmussen et al., 2007; Ślubowska-Woldengen et al., 2007; Ślubowska et al., 2005). Collectively, the measured authigenic ε_{Nd} signatures in leached Fe oxide fractions suggest a terrestrial origin sourced from subglacial to deglacial meltwater.

On this basis, we infer that the radiogenic authigenic ε_{Nd} peak of −10.8 (and the associated high $\Delta\varepsilon_{Nd}$ value) that occurred at ca. 1.4 ka BP (Fig. 4) reflects an increase in the glacier extent on Svalbard during the late Holocene (Dowdeswell et al., 2020; Kempf et al., 2013; Martín-Moreno et al., 2017) (Fig. 7B). At that time, the increased glacial abrasion induced by the growth of glaciers would have provided freshly exposed rock substrates and would have been followed by the preferential dissolution of easily dissolvable rock minerals during chemical weathering, resulting in an enhanced isotopic decoupling of Nd between solutes and source rocks, i.e., a higher $\Delta\varepsilon_{Nd}$ (Jang et al., 2020) (Fig. 7A). Similar increases in $\Delta\varepsilon_{Nd}$ during the late Holocene have been found in sediment cores retrieved from Woodfjorden (HH12–964) and Dicksonfjorden (HH16–1202) (Jang et al., 2020) (for locations, see Fig. 1). While the $\Delta\varepsilon_{Nd}$ values of core 1085-GC are slightly lower than those for two other nearby sites investigated by Jang et al. (2020), all records display a similar temporal evolution during the late Holocene, suggesting very similar glacial histories at that time.

Aside from the high $\Delta\varepsilon_{Nd}$ values during the late Holocene, an outstanding feature of our results is the seesaw fluctuations displayed by authigenic ε_{Nd} during the early deglaciation (−12.5 ± 0.8, 1σ, $n = 7$)
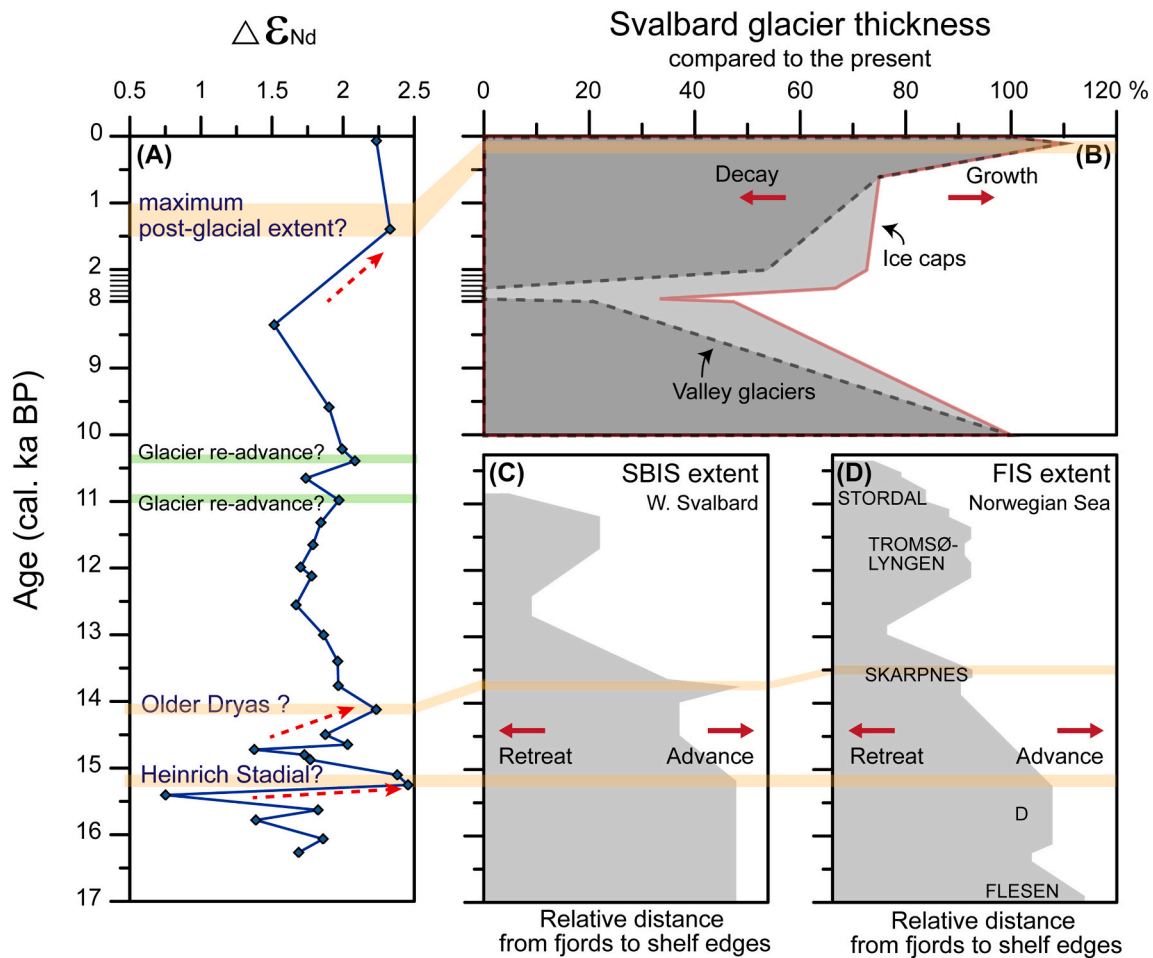
Fig. 7. (A) Differences between the authigenic and detrital ε_{Nd} values ($\Delta\varepsilon_{Nd}$) at the site of core HH17–1085-GC, (B) the modeled extent of Svalbard glaciers (Fjeldskaar et al., 2018), and the reconstructed extents of (C) the Svalbard-Barents Sea Ice Sheet (SBIS) in western Svalbard (Ebbesen et al., 2007; Elverhøi et al., 1995; Svendsen et al., 1996) and (D) the Fennoscandian Ice Sheet (FIS) in the Andfjord-Vågsfjord area in northern Norway (Vorren and Plassen, 2002). Three $\Delta\varepsilon_{Nd}$ peaks beyond the general uncertainty (~0.5 units) calculated by Monte-Carlo simulation (2σ, $n = 10,000$) (dashed red arrows) are marked by light orange bars and correlate with the glacial instability. Light green bars indicate minor $\Delta\varepsilon_{Nd}$ peaks, which may reflect glacier re-advances during the early Holocene. Five major glacial events for FIS are marked within the gray shaded area in (D). (For interpretation of the references to colour in this figure legend, the reader is referred to the web version of this article.)

(Fig. 4). Detrital ε_{Nd} values were almost constant (-14.3 ± 0.3, 1σ, $n = 7$) during this period; thus, these fluctuations most likely indicate variations in the degree of Nd isotopic decoupling in response to abruptly changing glacial activity and associated chemical weathering patterns. The maximum $\Delta\varepsilon_{Nd}$ values observed at ca. 15.2 ka BP could reflect pronounced ice sheet instability at that time associated with the incipient stage of ice sheet recession as recorded in the cores from offshore western Svalbard (Ebbesen et al., 2007; Elverhøi et al., 1995; Jessen et al., 2010; Svendsen et al., 1996) (Fig. 7C) and from sites offshore northern Norway (Vorren and Plassen, 2002) (Fig. 7D). The major recession of ice sheets (e.g., Hogan et al., 2017) or re-advances (e.g., the D-event in the European Arctic; Vorren and Plassen, 2002) probably supplied substantial fresh rock substrates available for intensifying the weathering of rock-forming minerals and the release of radiogenic isotopic signatures. Following an early stage characterized by intense incongruent weathering processes under unstable ice sheet conditions, the $\Delta\varepsilon_{Nd}$ signal would have returned smaller values as chemical weathering becomes more congruent (e.g., Jang et al., 2020; Süfke et al., 2019). Likewise, the subsequent increase in $\Delta\varepsilon_{Nd}$ observed during the late deglaciation (ca. 14.1 ka BP; Fig. 7A) would be related to significant ice sheet instability, perhaps in response to the increase in the Atlantic inflow (Ślubowska et al., 2005). This event could have occurred slightly after the Older Dryas period when the glacial re-advance was short-

lived, as documented in western Svalbard (Ebbesen et al., 2007; Elverhøi et al., 1995; Svendsen et al., 1996) (Fig. 7C) and the European Arctic regions (the Skarpnes-event; Vorren and Plassen, 2002) (Fig. 7D).

The results of our application of Nd isotopes in leached authigenic fractions suggest that the recession of glaciers on Svalbard progressed through a series of abrupt episodes of glacial retreat/advance rather than occurring gradually throughout the deglaciation period. The deglaciation of northern Svalbard was interrupted at least twice by short-term periods of glacial advances, similar to what has occurred in western Svalbard (Ebbesen et al., 2007; Elverhøi et al., 1995; Svendsen et al., 1996) and the European Arctic (Vorren and Plassen, 2002). The moderate increases in $\Delta\varepsilon_{Nd}$ (Fig. 7A) may be synchronous with glacier re-advances during the early Holocene (Farnsworth et al., 2020 and references therein); however, we found no $\Delta\varepsilon_{Nd}$ peak during the middle Holocene when glacier re-advances occurred (Baeten et al., 2010; Forwick et al., 2010; Jang et al., 2020; Svendsen and Mangerud, 1997; van der Bilt et al., 2015) (Fig. 8), probably due to sediment starvation at the site of core 1085-GC (Fig. 4).

7. Conclusion

Multi-proxy analyses of sediment core 1085-GC from the continental margin offshore northern Svalbard, including the novel use of Nd
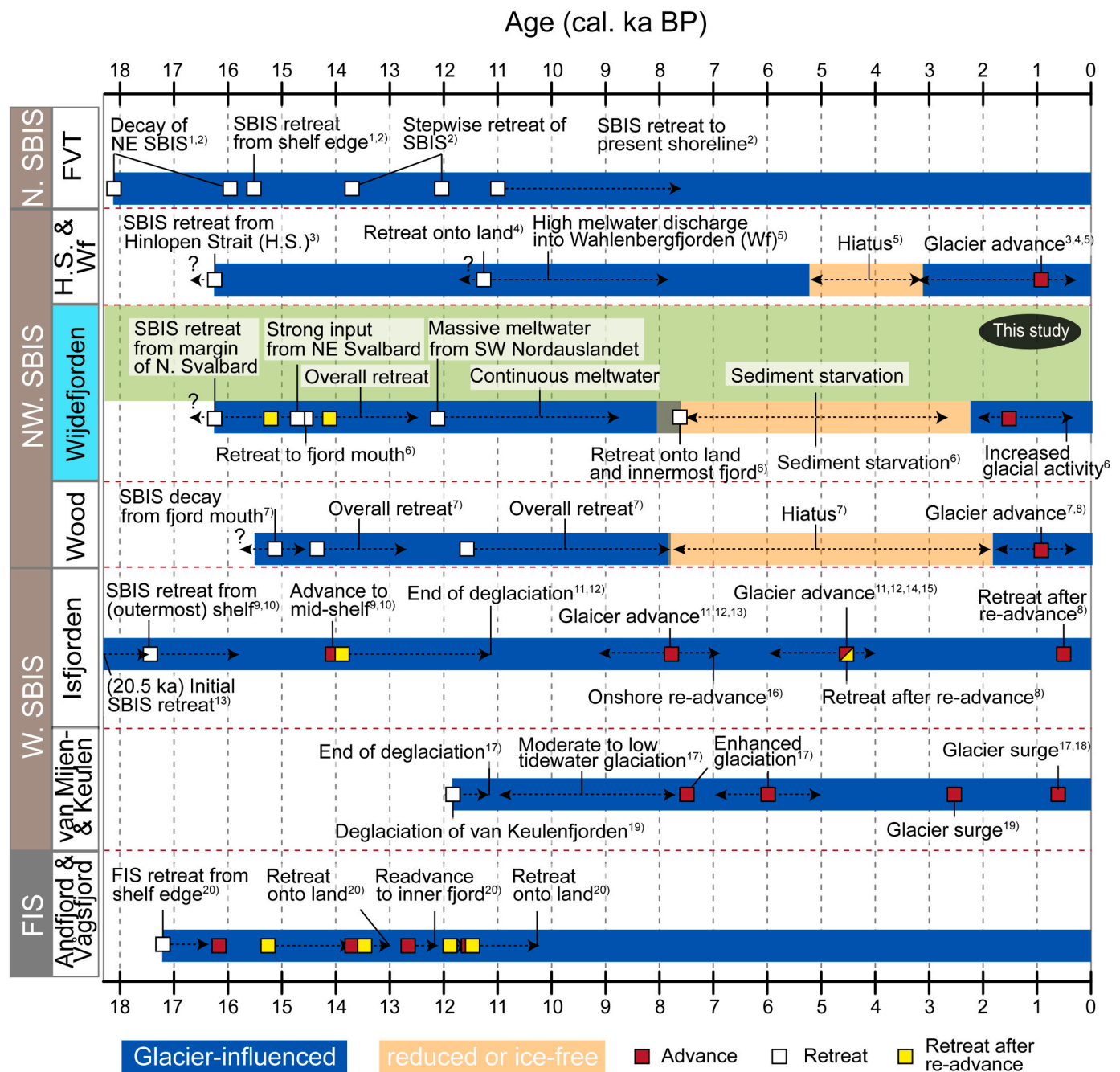
Fig. 8. Suggested timeline for the glacial history of northern Svalbard since the last deglaciation. Our results were compared with previous observations from the Franz Victoria Trough (FVT), Hinlopen Strait (H.S.), Wahlenbergfjorden (Wf), Wijdefjorden, Woodfjorden, and Isfjorden in Svalbard and Andfjord and Vågsfjord in Norway. References: [1] Knies et al. (2001), [2] Kleiber et al. (2000), [3] Koç et al. (2002), [4] Flink et al. (2017), [5] Bartels et al. (2018), [6] Allaart et al. (2020), [7] Bartels et al. (2017), [8] Jang et al. (2020), [9] Svendsen et al. (1996), [10] Elverhøi et al. (1995), [11] Forwick and Vorren (2009), [12] Baeten et al. (2010), [13] Jessen et al. (2010), [14] Svendsen and Mangerud (1997), [15] Forwick et al. (2010), [16] Forwick and Vorren (2007), [17] Hald et al. (2004), [18] Hald et al. (2001), [19] Kempf et al. (2013), [20] Vorren and Plassen (2002). (For interpretation of the references to colour in this figure legend, the reader is referred to the web version of this article.)

isotopes in both detrital and authigenic fractions as tracers of glacial weathering, provide new constraints on the dynamics of the SBIS and glaciers during and after the last deglaciation. Changing sediment provenance and chemical weathering signals indicate that the SBIS probably persisted longer on the northeastern margin of Svalbard than on the northwestern margin and that the deglaciation period in northern Svalbard was punctuated by at least two glacier re-advances at ca. 15.2 and 14.1 ka BP (Fig. 8). This stepwise deglaciation correlates with reconstructions from western Svalbard and northern Norway (Fig. 8), implying that the pronounced large-scale ice sheet dynamics in Svalbard

and Fennoscandia were synchronous during the last deglaciation. Glaciers on northern Svalbard underwent changes in extent during the Holocene, including major retreats during the early Holocene and re-advances during the late Holocene. Our study underlines the potential of employing Nd isotopes in both authigenic and detrital fractions for reconstructing the evolution of past ice sheets and glacier activity.

Data availability

The data are available within the paper and its supplementary

information files.

Declaration of Competing Interest

The authors declare that they have no known competing financial interests or personal relationships that could have appeared to influence the work reported in this paper.

Acknowledgments

Appendix A. Supplementary data

Supplementary data to this article can be found online at https://doi.org/10.1016/j.gloplacha.2021.103483.

References

Allaart, L., Müller, J., Schomacker, A., Rydningen, T.A., Håkansson, L., Kjellman, S.E., Mollenhauer, G., Forwick, M., 2020. Late Quaternary glacier and sea-ice history of northern Wijdefjorden, Svalbard. Boreas. https://doi.org/10.1111/bor.12435.

Baeten, N.J., Forwick, M., Vogt, C., Vorren, T.O., 2010. Late Weichselian and Holocene sedimentary environments and glacial activity in Billefjorden, Svalbard. Geol. Soc. Lond., Spec. Publ. 344, 207–223.

Bartels, M., Titschack, J., Fahl, K., Stein, R., Seidenkrantz, M.-S., Hillaire-Marcel, C., Hebbeln, D., 2017. Atlantic Water advection vs. glacier dynamics in northern Spitsbergen since early deglaciation. Clim. Past 13, 1717–1749.

Bartels, M., Titschack, J., Fahl, K., Stein, R., Hebbeln, D., 2018. Wahlenbergfjord, eastern Svalbard: a glacier-surrounded fjord reflecting regional hydrographic variability during the Holocene? Boreas 47, 1003–1021.

Batchelor, C.L., Dowdeswell, J.A., Hogan, K.A., 2011. Late Quaternary ice flow and sediment delivery through Hinlopen Trough, Northern Svalbard margin: Submarine landforms and depositional fan. Mar. Geol. 284, 13–27.

Bayon, G., German, C.R., Burton, K.W., Nesbitt, R.W., Rogers, N., 2004. Sedimentary Fe-Mn oxyhydroxides as paleoceanographic archives and the role of aeolian flux in regulating oceanic dissolved REE. Earth Planet. Sci. Lett. 224, 477–492.

Bayon, G., Barrat, J.A., Etoubleau, J., Benoit, M., Bollinger, C., Révillon, S., 2009. Determination of rare earth elements, Sc, Y, Zr, Ba, Hf and Th in geological samples by ICP-MS after Tm addition and alkaline fusion. Geostand. Geoanal. Res. 33, 51–62.

Bayon, G., Lambert, T., Vigier, N., De Deckker, P., Freslon, N., Jang, K., Larkin, C.S., Piotrowski, A.M., Tachikawa, K., Thollon, M., Tipper, E.T., 2020. Rare earth element and neodymium isotope tracing of sedimentary rock weathering. Chem. Geol. 553, 119794.

Berben, S.M., Husum, K., Navarro-Rodriguez, A., Belt, S.T., Aagaard-Sørensen, S., 2017. Semi-quantitative reconstruction of early to late Holocene spring and summer sea ice conditions in the northern Barents Sea. J. Quat. Sci. 32, 587–603.

Blaauw, M., Christen, J.A., 2011. Flexible paleoclimate age-depth models using an autoregressive gamma process. Bayesian Anal. 6, 457–474.

Blomeier, D., Wisshak, M., Dallmann, W., Volohonsky, E., Freiwald, A., 2003a. Facies analysis of the Old Red Sandstone of Spitsbergen (Wood Bay Formation): reconstruction of the depositional environments and implications of basin development. Facies 49, 151–174.

Blomeier, D., Wisshak, M., Joachimski, M., Freiwald, A., Volohonsky, E., 2003b. Calcareous, alluvial and lacustrine deposits in the Old Red Sandstone of central north Spitsbergen (Wood Bay Formation, Early Devonian). Nor. J. Geol. 83, 281–298.

Blomeier, D., Dustira, A., Forke, H., Scheibner, C., 2011. Environmental change in the early Permian of NE Svalbard: from a warm-water carbonate platform (Gipshuken Formation) to a temperate, mixed siliciclastic-carbonate ramp (Kapp Starostin Formation). Facies 57, 493–523.

Blott, S.J., Pye, K., 2001. GRADISTAT: a grain size distribution and statistics package for the analysis of unconsolidated sediments. Earth Surf. Process. Landf. 26, 1237–1248.

Böhm, E., Lippold, J., Gutjahr, M., Frank, M., Blaser, P., Antz, B., Fohlmeister, J., Frank, N., Andersen, M., Deininger, M., 2015. Strong and deep Atlantic meridional overturning circulation during the last glacial cycle. Nature 517, 73–76.

Bond, D.P., Blomeier, D.P., Dustira, A.M., Wignall, P.B., Collins, D., Goode, T., Groen, R. D., Buggisch, W., Grasby, S.E., 2018. Sequence stratigraphy, basin morphology and sea-level history for the Permian Kapp Starostin Formation of Svalbard, Norway. Geol. Mag. 155, 1023–1039.

Braun, C., 2019. Late Weichselian and Holocene Glacier Dynamics and Sedimentary Processes in and North of the Wijdefjorden-Austfjorden Fjord System, North Spitsbergen. The Arctic University of Norway.

Chen, T.-Y., Frank, M., Haley, B.A., Gutjahr, M., Spielhagen, R.F., 2012. Variations of North Atlantic inflow to the Central Arctic Ocean over the last 14 million years inferred from hafnium and neodymium isotopes. Earth Planet. Sci. Lett. 353, 82–92.

Cottier, F., Tverberg, V., Inall, M., Svendsen, H., Nilsen, F., Griffiths, C., 2005. Water mass modification in an Arctic fjord through cross-shelf exchange: the seasonal hydrography of Kongsfjorden, Svalbard. J. Geophys. Res. Oceans 110, C12005.

Curry, J.A., Schramm, J.L., Ebert, E.E., 1995. Sea ice-albedo climate feedback mechanism. J. Clim. 8, 240–247.

Dallmann, W.K., 2015. Geoscience Atlas of Svalbard, 148. Norsk Polarinst, Tromsø, p. 292.

Darby, D.A., Polyak, L., Bauch, H.A., 2006. Past glacial and interglacial conditions in the Arctic Ocean and marginal seas - a review. Prog. Oceanogr. 71, 129–144.

Dowdeswell, J.A., Hogan, K.A., Evans, J., Noormets, R., ÓCofaigh, C., Ottesen, D., 2010. Past ice-sheet flow east of Svalbard inferred from streamlined subglacial landforms. Geology 38, 163–166.

Dowdeswell, J.A., Ottesen, D., Bellec, V.K., 2020. The changing extent of marine-terminating glaciers and ice caps in northeastern Svalbard since the 'Little Ice Age' from marine-geophysical records. The Holocene 30, 389–401.

Ebbesen, H., Hald, M., Eplet, T.H., 2007. Lateglacial and early Holocene climatic oscillations on the western Svalbard margin, European Arctic. Quat. Sci. Rev. 26, 1999–2011.

Elverhøi, A., Andersen, E.S., Dokken, T., Hebbeln, D., Spielhagen, R., Svendsen, J.I., Sørflaten, M., Rørnes, A., Hald, M., Forsberg, C.F., 1995. The growth and decay of the late Weichselian ice sheet in western Svalbard and adjacent areas based on provenance studies of marine sediments. Quat. Res. 44, 303–316.

Farnsworth, W.R., Allaart, L., Ingólfsson, Ó., Alexanderson, H., Forwick, M., Noormets, R., Retelle, M., Schomacker, A., 2020. Holocene glacial history of Svalbard: Status, perspectives and challenges. Earth-Sci. Rev. 208, 103249.

Fjeldskaar, W., Bondevik, S., Amantov, A., 2018. Glaciers on Svalbard survived the Holocene thermal optimum. Quat. Sci. Rev. 199, 18–29.

Flink, A.E., Noormets, R., Fransner, O., Hogan, K.A., ÓRegan, M., Jakobsson, M., 2017. Past ice flow in Wahlenbergfjorden and its implications for late Quaternary ice sheet dynamics in northeastern Svalbard. Quat. Sci. Rev. 163, 162–179.

Folk, R.L., Ward, W.C., 1957. Brazos River bar [Texas]; a study in the significance of grain size parameters. J. Sediment. Res. 27, 3–26.

Forman, S., Lubinski, D., Ingólfsson, Ó., Zeeberg, J., Snyder, J., Siegert, M., Matishov, G., 2004. A review of postglacial emergence on Svalbard, Franz Josef Land and Novaya Zemlya, northern Eurasia. Quat. Sci. Rev. 23, 1391–1434.

Fortey, R.A., Bruton, D.L., 1973. Cambrian-Ordovician rocks adjacent to Hinlopenstretet, north Ny Friesland, Spitsbergen. Geol. S. Am. Bull. 84, 2227–2242.

Forwick, M., Vorren, T.O., 2007. Holocene mass-transport activity and climate in outer Isfjorden, Spitsbergen: marine and subsurface evidence. The Holocene 17, 707–716.

Forwick, M., Vorren, T.O., 2009. Late Weichselian and Holocene sedimentary environments and ice rafting in Isfjorden, Spitsbergen. Palaeogeogr. Palaeoclimatol. Palaeoecol. 280, 258–274.

Forwick, M., Vorren, T.O., Hald, M., Korsun, S., Roh, Y., Vogt, C., Yoo, K.-C., 2010. Spatial and temporal influence of glaciers and rivers on the sedimentary environment in Sassenfjorden and Tempelfjorden, Spitsbergen. Geol. Soc. Lond., Spec. Publ. 344, 163–193.

Goldstein, S.L., Hemming, S.R., 2003. Long-lived isotopic tracers in oceanography, paleoceanography, and ice-sheet dynamics. In: Elderfield, H. (Ed.), Treatise on Geochemistry. Elsevier, Oxford, pp. 453–489.

Grousset, F., Biscaye, P., Zindler, A., Prospero, J., Chester, R., 1988. Neodymium isotopes as tracers in marine sediments and aerosols: North Atlantic. Earth Planet. Sci. Lett. 87, 367–378.

Haley, B.A., Polyak, L., 2013. Pre-modern Arctic Ocean circulation from surface sediment neodymium isotopes. Geophys. Res. Lett. 40, 893–897.

Hald, M., Dahlgren, T., Olsen, T.-E., Lebesbye, E., 2001. Late Holocene palaeoceanography in Van Mijenfjorden, Svalbard. Polar Res. 20, 23–35.

Hald, M., Ebbesen, H., Forwick, M., Godtliebsen, F., Khomenko, L., Korsun, S., Olsen, L. R., Vorren, T.O., 2004. Holocene paleoceanography and glacial history of the West Spitsbergen area, Euro-Arctic margin. Quat. Sci. Rev. 23, 2075–2088.

Hindshaw, R.S., Aciego, S.M., Piotrowski, A.M., Tipper, E.T., 2018. Decoupling of dissolved and bedrock neodymium isotopes during sedimentary cycling. Geochem. Perspect. Lett. 8, 43–46.

Hjelle, A., 1993. Geology of Svalbard. Norsk Polarinsti, Oslo, p. 163.

Hogan, K.A., Dowdeswell, J.A., Hillenbrand, C.-D., Ehrmann, W., Noormets, R., Wacker, L., 2017. Subglacial sediment pathways and deglacial chronology of the northern Barents Sea Ice Sheet. Boreas 46, 750–771.

Horikawa, K., Martin, E.E., Basak, C., Onodera, J., Seki, O., Sakamoto, T., Ikehara, M., Sakai, S., Kawamura, K., 2015. Pliocene cooling enhanced by flow of low-salinity Bering Sea water to the Arctic Ocean. Nat. Commun. 6 https://doi.org/10.1038/ncomms8587.

Hormes, A., Akçar, N., Kubik, P.W., 2011. Cosmogenic radionuclide dating indicates ice-sheet configuration during MIS 2 on Nordaustlandet, Svalbard. Boreas 40, 636–649.

Hughes, A.L., Gyllencreutz, R., Lohne, Ø.S., Mangerud, J., Svendsen, J.I., 2016. The last Eurasian ice sheets–a chronological database and time-slice reconstruction, DATED-1. Boreas 45, 1–45.

Jacobsen, S.B., Wasserburg, G.J., 1980. Sm-Nd isotopic evolution of chondrites. Earth Planet. Sci. Lett. 50, 139–155.

Jakobsson, M., Andreassen, K., Bjarnadóttir, L.R., Dove, D., Dowdeswell, J.A., England, J.H., Funder, S., Hogan, K., Ingólfsson, Ó., Jennings, A., Krog Larsen, N., Kirchner, N., Landvik, J.Y., Mayer, L., Mikkelsen, N., Möller, P., Niessen, F., Nilsson, J., O'Regan, M., Polyak, L., Nørgaard-Pedersen, N., Stein, R., 2014. Arctic Ocean glacial history. Quat. Sci. Rev. 92, 40–67.

Jang, K., Han, Y., Huh, Y., Nam, S.-I., Stein, R., Mackensen, A., Matthiessen, J., 2013. Glacial freshwater discharge events recorded by authigenic neodymium isotopes in sediments from the Mendeleev Ridge, western Arctic Ocean. Earth Planet. Sci. Lett. 369-370, 148–157.

Jang, K., Huh, Y., Han, Y., 2017. Authigenic Nd isotope record of North Pacific Intermediate Water formation and boundary exchange on the Bering Slope. Quat. Sci. Rev. 156, 150–163.

Jang, K., Bayon, G., Han, Y., Joo, Y.J., Kim, J.-H., Ryu, J.-S., Woo, J., Forwick, M., Szczuciński, W., Kim, J.-H., Nam, S.-I., 2020. Neodymium isotope constraints on chemical weathering and past glacial activity in Svalbard. Earth Planet. Sci. Lett. 542, 116319.

Jernas, P., Klitgaard Kristensen, D., Husum, K., Wilson, L., Koç, N., 2013. Palaeoenvironmental changes of the last two millennia on the western and northern Svalbard shelf. Boreas 42, 236–255.

Jessen, S.P., Rasmussen, T.L., Nielsen, T., Solheim, A., 2010. A new late Weichselian and Holocene marine chronology for the western Svalbard slope 30,000–0 cal years BP. Quat. Sci. Rev. 29, 1301–1312.

Johansson, Å., Gee, D.G., 1999. The late Palaeoproterozoic Eskolabreen granitoids of southern Ny Friesland, Svalbard Caledonides-geochemistry, age, and origin. GFF 121, 113–126.

Johansson, Å., Gee, D., Björklund, L., Witt-Nilsson, P., 1995. Isotope studies of granitoids from the Bangenhuk formation, Ny Friesland Caledonides, Svalbard. Geol. Mag. 132, 303–320.

Johansson, Å., Larionov, A.N., Tebenkov, A.M., Gee, D.G., Whitehouse, M.J., Vestin, J., 2000. Grenvillian magmatism of western and central Nordaustlandet, northeastern Svalbard. Earth Environ. Sci. T. R. Soc. 90, 221–254.

Johansson, Å., Larionov, A.N., Tebenkov, A.M., Ohta, Y., Gee, D.G., 2002. Caledonian granites of western and central Nordaustlandet, Northeast Svalbard. GFF 124, 135–148.

Jonkers, L., Zahn, R., Thomas, A., Henderson, G., Abouchami, W., François, R., Masque, P., Hall, I.R., Bickert, T., 2015. Deep circulation changes in the central South Atlantic during the past 145 kyrs reflected in a combined $^{231}Pa/^{230}Th$, neodymium isotope and benthic $\delta^{13}C$ record. Earth Planet. Sci. Lett. 419, 14–21.

Kempf, P., Forwick, M., Laberg, J.S., Vorren, T.O., 2013. Late Weichselian and Holocene sedimentary palaeoenvironment and glacial activity in the high-arctic van Keulenfjorden, Spitsbergen. The Holocene 23, 1607–1618.

Kleiber, H., Knies, J., Niessen, F., 2000. The late Weichselian glaciation of the Franz Victoria Trough, northern Barents Sea: ice sheet extent and timing. Mar. Geol. 168, 25–44.

Knies, J., Martinez, P., 2009. Organic matter sedimentation in the western Barents Sea region: Terrestrial and marine contribution based on isotopic composition and organic nitrogen content. Nor. J. Geol. 89, 79–89.

Knies, J., Kleiber, H.-P., Matthiessen, J., Müller, C., Nowaczyk, N., 2001. Marine ice-rafted debris records constrain maximum extent of Saalian and Weichselian ice-sheets along the northern Eurasian margin. Glob. Planet. Chang. 31, 45–64.

Koç, N., Klitgaard-Kristensen, D., Hasle, K., Forsberg, C.F., Solheim, A., 2002. Late glacial palaeoceanography of Hinlopen Strait, northern Svalbard. Polar Res. 21, 307–314.

Kunzmann, M., Halverson, G.P., Scott, C., Minarik, W.G., Wing, B.A., 2015. Geochemistry of Neoproterozoic black shales from Svalbard: Implications for oceanic redox conditions spanning Cryogenian glaciations. Chem. Geol. 417, 383–393.

Landvik, J.Y., Bondebik, S., Elyerhoi, A., Fjeldskaar, W., Mangerud, J., Siegert, S., Salvigsen, O., Svendsen, J.-I., Vorren, T.O., 1998. The last glacial maximum of Svalbard and the Barents Sea area: ice sheet extent and configuration. Quat. Sci. Rev. 17, 43–76.

Laukert, G., Frank, M., Bauch, D., Hathorne, E.C., Rabe, B., von Appen, W.-J., Wegner, C., Zieringer, M., Kassens, H., 2017. Ocean circulation and freshwater pathways in the Arctic Mediterranean based on a combined Nd isotope, REE and oxygen isotope section across Fram Strait. Geochim. Cosmochim. Acta 202, 285–309.

Lauritzen, Ø., 1981. Investigations of Carboniferous and Permian Sediments in Svalbard, 176. Norsk Polarinsti. Skri, p. 47.

Maccali, J., Hillaire-Marcel, C., Carignan, J., Reisberg, L.C., 2013. Geochemical signatures of sediments documenting Arctic Sea-ice and water mass export through Fram Strait since the Last Glacial Maximum. Quat. Sci. Rev. 64, 136–151.

Mackiewicz, N.E., Powell, R.D., Carlson, P.R., Molnia, B.F., 1984. Interlaminated ice-proximal glacimarine sediments in Muir Inlet, Alaska. Mar. Geol. 57, 113–147.

Mangerud, J., Bondevik, S., Gulliksen, S., Karin Hufthammer, A., Høisæter, T., 2006. Marine ^{14}C reservoir ages for 19th century whales and molluscs from the North Atlantic. Quat. Sci. Rev. 25, 3228–3245.

Martín-Moreno, R., Allende Álvarez, F., Hagen, J.O., 2017. 'Little Ice Age' glacier extent and subsequent retreat in Svalbard archipelago. The Holocene 27, 1379–1390.

Menze, S., Ingvaldsen, R.B., Haugan, P., Fer, I., Sundfjord, A., Beszczynska-Moeller, A., Falk-Petersen, S., 2019. Atlantic water pathways along the North-Western Svalbard shelf mapped using vessel-mounted current profilers. J. Geophys. Res. Oceans 124, 1699–1716.

Moore, D.M., Reynolds Jr., R.C., 1989. X-ray Diffraction and the Identification and Analysis of Clay Minerals. Oxford University Press (OUP), pp. 179–201.

Nuth, C., Kohler, J., König, M., Deschwanden, A.v., Hagen, J.O.M., Kääb, A., Moholdt, G., Pettersson, R., 2013. Decadal changes from a multi-temporal glacier inventory of Svalbard. Cryosphere 7, 1603–1621.

ÓCofaigh, C., Dowdeswell, J.A., 2001. Laminated sediments in glacimarine environments: diagnostic criteria for their interpretation. Quat. Sci. Rev. 20, 1411–1436.

Ottesen, D., Dowdeswell, J.A., Landvik, J.Y., Mienert, J., 2007. Dynamics of the late Weichselian ice sheet on Svalbard inferred from high-resolution sea-floor morphology. Boreas 36, 286–306.

Patton, H., Hubbard, A., Andreassen, K., Winsborrow, M., Stroeven, A.P., 2016. The build-up, configuration, and dynamical sensitivity of the Eurasian ice-sheet complex to late Weichselian climatic and oceanic forcing. Quat. Sci. Rev. 153, 97–121.

Patton, H., Hubbard, A., Andreassen, K., Auriac, A., Whitehouse, P.L., Stroeven, A.P., Shackleton, C., Winsborrow, M., Heyman, J., Hall, A.M., 2017. Deglaciation of the Eurasian ice sheet complex. Quat. Sci. Rev. 169, 148–172.

Pereira, P.S., Flierdt, T.V.D., Hemming, S.R., Frederichs, T., Hammond, S.J., Brachfeld, S., Doherty, C., Kuhn, G., Smith, J.A., Klages, J.P., Hillenbrand, C.-D., 2020. The geochemical and mineralogical fingerprint of West Antarctica's weak underbelly: Pine Island and Thwaites glaciers. Chem. Geol. 550, 119649.

Petschick, R., Kuhn, G., Gingele, F., 1996. Clay mineral distribution in surface sediments of the South Atlantic: sources, transport, and relation to oceanography. Mar. Geol. 130, 203–229.

Pfirman, S., Colony, R., Nürnberg, D., Eicken, H., Rigor, I., 1997. Reconstructing the origin and trajectory of drifting Arctic sea ice. J. Geophys. Res. Oceans 102, 12575–12586.

Pin, C., Zalduegui, J.S., 1997. Sequential separation of light rare-earth elements, thorium and uranium by miniaturized extraction chromatography: Application to isotopic analyses of silicate rocks. Anal. Chim. Acta 339, 79–89.

Piotrowski, A.M., Goldstein, S.L., Hemming, S.R., Fairbanks, R.G., 2005. Temporal relationships of carbon cycling and ocean circulation at glacial boundaries. Science 307, 1933–1938.

R Core Team, 2020. R: A language and environment for statistical computing. R Foundation for Statistical Computing, Austria, Vienna. https://www.R-project.org/.

Raczek, I., Jochum, K.P., Hofmann, A.W., 2003. Neodymium and strontium isotope data for USGS reference materials BCR-1, BCR-2, BHVO-1, BHVO-2, AGV-1, AGV-2, GSP-1, GSP-2 and eight MPI-DING reference glasses. Geostand. Newslett. 27, 173–179.

Rahaman, W., Smik, L., Köseoğlu, D., Lathika, N., Tarique, M., Thamban, M., Haywood, A., Belt, S.T., Knies, J., 2020. Reduced Arctic sea ice extent during the mid-Pliocene warm period concurrent with increased Atlantic-climate regime. Earth Planet. Sci. Lett. 550, 116535.

Rasmussen, T.L., Thomsen, E., 2013. Pink marine sediments reveal rapid ice melt and Arctic meltwater discharge during Dansgaard–Oeschger warmings. Nat. Commun. 4, 1–8.

Rasmussen, T.L., Thomsen, E., 2014. Brine formation in relation to climate changes and ice retreat during the last 15,000 years in Storfjorden, Svalbard, 76–78 N. Paleoceanography 29, 911–929.

Rasmussen, T.L., Thomsen, E., Ślubowska, M.A., Jessen, S., Solheim, A., Koç, N., 2007. Paleoceanographic evolution of the SW Svalbard margin (76°N) since 20,000 ^{14}C yr BP. Quat. Res. 67, 100–114.

Revel, M., Sinko, J.A., Grousset, F.E., Biscaye, P.E., 1996. Sr and Nd isotopes as tracers of North Atlantic lithic particles: Paleoclimatic implications. Paleoceanography 11, 95–113.

Røthe, T.O., Bakke, J., Vasskog, K., Gjerde, M., D'Andrea, W.J., Bradley, R.S., 2015. Arctic Holocene glacier fluctuations reconstructed from lake sediments at Mitrahalvøya, Spitsbergen. Quat. Sci. Rev. 109, 111–125.

Rutberg, R.L., Hemming, S.R., Goldstein, S.L., 2000. Reduced North Atlantic Deep Water flux to the glacial Southern Ocean inferred from neodymium isotope ratios. Nature 405, 935–938.

Silva, J.A., Bremner, J.M., 1966. Determination and isotope-ratio analysis of different forms of nitrogen in soils: 5. Fixed Ammonium. Soil Sci. Soc. Am. J. 30, 587–594.

Ślubowska, M.A., Koç, N., Rasmussen, T.L., Klitgaard-Kristensen, D., 2005. Changes in the flow of Atlantic water into the Arctic Ocean since the last deglaciation: evidence from the northern Svalbard continental margin, 80°N. Paleoceanography 20. https://doi.org/10.1029/2005PA001141.

Ślubowska-Woldengen, M., Rasmussen, T.L., Koç, N., Klitgaard-Kristensen, D., Nilsen, F., Solheim, A., 2007. Advection of Atlantic Water to the western and northern Svalbard shelf since 17,500 cal yr BP. Quat. Sci. Rev. 26, 463–478.

Stein, R., 2019. The late Mesozoic-Cenozoic Arctic Ocean climate and sea ice history: a challenge for past and future scientific ocean drilling. Paleoceanogr. Paleoclimatol. 34, 1851–1894.

Stuiver, M., Reimer, P.J., 1993. Extended ^{14}C data base and revised CALIB 3.0 ^{14}C age calibration program. Radiocarbon 35, 215–230.

Süfke, F., Gutjahr, M., Gilli, A., Anselmetti, F.S., Glur, L., Eisenhauer, A., 2019. Early stage weathering systematics of Pb and Nd isotopes derived from a high-Alpine Holocene lake sediment record. Chem. Geol. 507, 42–53.

Svendsen, J.I., Mangerud, J., 1997. Holocene glacial and climatic variations on Spitsbergen, Svalbard. The Holocene 7, 45–57.

Svendsen, J.I., Mangerud, J., Elverhøi, A., Solheim, A., Schüttenhelm, R.T., 1992. The late Weichselian glacial maximum on western Spitsbergen inferred from offshore sediment cores. Mar. Geol. 104, 1–17.

Svendsen, J.I., Elverhøi, A., Mangerud, J., 1996. The retreat of the Barents Sea Ice Sheet on the western Svalbard margin. Boreas 25, 244–256.

Svendsen, J.I., Alexanderson, H., Astakhov, V.I., Demidov, I., Dowdeswell, J.A., Funder, S., Gataullin, V., Henriksen, M., Hjort, C., Houmark-Nielsen, M., Hubberten, H.W., Ingólfsson, Ó., Jakobsson, M., Kjær, K.H., Larsen, E., Lokrantz, H., Lunkka, J.P., Lyså, A., Mangerud, J., Matiouchkov, A., Murray, A., Möller, P.,

Niessen, F., Nikolskaya, O., Polyak, L., Saarnisto, M., Siegert, C., Siegert, M.J., Spielhagen, R.F., Stein, R., 2004. Late Quaternary ice sheet history of northern Eurasia. Quat. Sci. Rev. 23, 1229–1271.

Tanaka, T., Togashi, S., Kamioka, H., Amakawa, H., Kagami, H., Hamamoto, T., Yuhara, M., Orihashi, Y., Yoneda, S., Shimizu, H., Kunimaru, T., Takahashi, K., Yanagi, T., Nakano, T., Fujimaki, H., Shinjo, R., Asahara, Y., Tanimizu, M., Dragusanu, C., 2000. JNdi-1: a neodymium isotopic reference in consistency with LaJolla neodymium. Chem. Geol. 168, 279–281.

Tarasov, L., Peltier, W., 2005. Arctic freshwater forcing of the Younger Dryas cold reversal. Nature 435, 662–665.

Teschner, C., Frank, M., Haley, B.A., Knies, J., 2016. Plio-Pleistocene evolution of water mass exchange and erosional input at the Atlantic-Arctic gateway. Paleoceanography 31, 582–599.

Tian, S.Y., Yasuhara, M., Hong, Y., Huang, H.-H.M., Iwatani, H., Chiu, W.-T.R., Mamo, B., Okahashi, H., Rasmussen, T.L., 2020. Deglacial–Holocene Svalbard paleoceanography and evidence of meltwater pulse 1B. Quat. Sci. Rev. 233, 106237.

Tütken, T., Eisenhauer, A., Wiegand, B., Hansen, B.T., 2002. Glacial–interglacial cycles in Sr and Nd isotopic composition of Arctic marine sediments triggered by the Svalbard/Barents Sea ice sheet. Mar. Geol. 182, 351–372.

van der Bilt, W.G.M., Bakke, J., Vasskog, K., D'Andrea, W.J., Bradley, R.S., Ólafsdóttir, S., 2015. Reconstruction of glacier variability from lake sediments reveals dynamic Holocene climate in Svalbard. Quat. Sci. Rev. 126, 201–218.

Vogt, C., Lauterjung, J.r., Fischer, R.X., 2002. Investigation of the clay fraction (< 2 μm) of the clay minerals society reference clays. Clays Clay Min. 50, 388–400.

Vorren, T.O., Plassen, L., 2002. Deglaciation and palaeoclimate of the Andfjord-Vågsfjord area, North Norway. Boreas 31, 97–125.

Werner, K., Frank, M., Teschner, C., Müller, J., Spielhagen, R.F., 2014. Neoglacial change in deep water exchange and increase of sea-ice transport through eastern Fram Strait: evidence from radiogenic isotopes. Quat. Sci. Rev. 92, 190–207.

Winkelmann, D., Knies, J., 2005. Recent distribution and accumulation of organic carbon on the continental margin west off Spitsbergen. Geochem. Geophys. Geosyst. 6.